Noise Prediction of Multi-stream Internally Mixed Jets with External and Internal Plugs using Large-Eddy Simulation

Gerrit-Daniel Stich *, Chase Ashby, †,
Olivia Martin ‡, Jeffrey A. Housman, § and Jared C. Duensing ¶
NASA Ames Research Center, M/S 258-2, Moffet Field, CA 94035

This paper presents results from ongoing research on jet noise prediction using wall-modeled large eddy simulations (WMLES) conducted within the Launch Ascent and Vehicle Aerodynamics (LAVA) computational framework. The study primarily focuses on the aeroacoustic implications of multi-stream nozzle configurations with internal mixing and both internal and external plugs, at a Reynolds number of 1×10^6 based on the nozzle exit diameter. While internal mixing nozzles have long been considered for jet noise reduction, the complexities of their impact on overall noise levels remain insufficiently understood. This research applies established best practices for WMLES to these complex nozzle configurations, aiming to assess their efficacy and identify limitations in accurately predicting noise behaviors. Through detailed comparisons with experimental data obtained from NASA's Glenn Research Center, initial findings underscore the challenges inherent in current simulation practices when confronted with intricate geometric and operational conditions. Responding to these challenges, the study explores innovative computational approaches to rectify discrepancies noted between experimental outcomes and CFD predictions. Once example is the introduction of a resonating sound source in the simulation environment to mimic potential unobserved acoustic phenomena. A second example is the strategic modifications to the geometry of external plugs to account for real-world deformations caused by heating and gravity. These novel strategies aim to enhance the accuracy and reliability of noise predictions from supersonic jets, advancing our understanding and capability to effectively reduce jet noise in commercial supersonic aircraft.

I. Introduction

The resurgence of interest in supersonic transport, spurred by advancements in aerospace technology, brings forward the longstanding challenge of noise mitigation during critical phases of flight such as landing and takeoff (LTO). The quest for efficient supersonic flight is often at odds with the requirements for quieter operations near urban areas, where noise regulations are stringent. NASA's Commercial Supersonic Technology (CST) project addresses these challenges by focusing on the development of propulsion systems that not only meet but exceed in undercutting current noise regulations [1]. This effort is vital as the acoustic impact of aircraft during LTO phases can significantly influence public acceptance and regulatory compliance of commercial supersonic operations. Dual-stream nozzle configurations, featuring distinct high and low-pressure air streams, have emerged as a critical area of focus. These configurations are integral to supersonic aircraft as they offer potential improvements in propulsion efficiency and noise characteristics. The design of these nozzles involves complex trade-offs: they must efficiently handle the high jet exit velocities required for supersonic cruise performance while minimizing the noise footprint during lower speed operations. The acoustic performance of these nozzles is influenced by several factors including the geometric design of the nozzle, the interaction between the high and low-pressure streams, and the methods used to mix these streams.

The traditional approach to managing jet noise has centered on optimizing the nozzle geometries to enhance turbulent mixing, which can help dissipate acoustic energy more effectively. However, nozzles equipped with features like a translating external plug or adjustable nozzle lips add layers of complexity. These features allow for dynamic changes in throat and exit areas, optimizing the aerodynamic performance across different flight regimes but also altering the acoustic signature in ways that are not fully understood. Such nozzles can adjust the effective boattail angle, which is the

*Science and Technology Corporation, AIAA Senior Member, gerrit-daniel.stich@nasa.gov
†Computational Aerosciences Branch, AIAA Member, chase.ashby@nasa.gov
‡Computational Aerosciences Branch, Stanford University, AIAA Member, olivia.martin@nasa.gov
§Computational Aerosciences Branch, AIAA Senior Member, jeffrey.a.housman@nasa.gov
¶Computational Aerosciences Branch, AIAA Member, jared.c.duensing@nasa.gov

angle of taper at the nozzle exit where the nozzle narrows or flares out. This angle is crucial for reducing sonic boom and drag in supersonic flight, but it also affects how noise propagates from the jet plume, particularly when compared to simpler internal plug nozzles [2].

Moreover, the presence of two distinct air streams in turbofan engines introduces additional complexities. In configurations where these streams are internally mixed, the design of the mixer—often a lobed or forced mixer—becomes a focal point for optimizing performance and noise. These mixers facilitate the rapid blending of the core and bypass streams, theoretically leading to a more uniform exit flow and potentially quieter operation. However, the reality is nuanced; the degree of mixing and the resultant flow uniformity can significantly affect the noise generated. Incomplete mixing, characterized by high-speed streaks and other flow irregularities (such as turbulence, vortices, shock waves, separation bubbles, and instabilities), can introduce additional noise sources, making the jet plume acoustically harsher [2]. Historical and ongoing research underscores the need for a deeper understanding of these interactions. While previous studies have laid a solid foundation in fluid mechanics, the acoustic implications of advanced mixer designs and dual-stream interactions remain an area ripe for further exploration. This is particularly true in the context of supersonic transport, where the operational demands and environmental constraints necessitate innovative approaches to noise reduction [3].

Over the past decades, Computational Fluid Dynamics (CFD) has been crucial in predicting jet noise, with significant progress made towards incorporating complex geometrical features such as jet surface interactions [4–6]. Despite these advancements, the complexity of full-scale airframe interactions continues to make such simulations computationally demanding and resource-intensive. Addressing the complexities inherent in dual-stream nozzle configurations necessitates advanced computational techniques capable of handling the intricate geometries and flow interactions typical of such systems. Wall-modeled large eddy simulation (WMLES) offers a practical solution by reducing computational overhead without sacrificing the granularity required for accurate noise prediction. Within NASA's Launch, Ascent, and Vehicle Aerodynamics (LAVA) framework, WMLES is employed to model the aeroacoustic behaviors of multi-stream internally mixed nozzles with external plugs. This framework has proven effective in simulating complex aerodynamic and aeroacoustic problems across relevant flight conditions [5, 7, 8].

This study is divided in two parts and outlines our preliminary findings form this ongoing study. Part I (Section V) of this study focuses on benchmarking the CFD results against experimental data, including both near-field flow characteristics captured through Particle Image Velocimetry (PIV) and far-field noise measurements. We will utilize best practices developed for simpler canonical round jets as reported in previous studies [8–10] as well as in literature [4, 11–13] and assess it's performance for four different configurations. The set of configurations are labeled further as the plug20 nozzle dataset as described in Bridges et.al [2, 3, 14]. We will provide comparisons between CFD results and experimental data, focusing on both near-field comparisons with Particle Image Velocimetry (PIV) and far-field noise from microphone measurements. From here we will assess standard best practices and assess potential noise differences.

Part II (Section VI) will explore investigative approaches to reconcile observed discrepancies, such as adjusting turbulence inflow states, and modifying nozzle plug geometries. In addition we introduce an immersed boundary method (IB) approach utilizing a penatly source term method in order to alleviate the meshing constraints for complex mixer geometries. This dual-focused study aims to refine the predictive capabilities of CFD models for supersonic jet noise, ultimately contributing to the development of quieter propulsion systems for commercial supersonic aircraft. The insights gained and a better understanding of the uncertainties within this prediction method will inform future aircraft designs and regulatory standards for supersonic transport noise.

Finally, in Section VII, we introduce a novel meshing and solution approach that significantly accelerates the testing of various mixer configurations. This method automates the complex time consuming manual meshing process by integrating an immersed boundary penalty method with adaptive curvilinear mesh refinement, effectively reducing turnaround times.

II. Problem Description

The corresponding experiments were conducted at the Small Hot Jet Acoustic Rig (SHJAR), which is located in the Aeroacoustic Propulsion Laboratory (AAPL) at NASA Glenn Research Center [15]. The SHJAR was commissioned in 2001 to test jet noise reduction concepts and develop advanced measurement techniques and is capable of supplying air at flow rates up to 2.7 kg/s to a single-nozzle stream. Details of the SHJAR, the measurement techniques used to acquire the near-field and far-field data, and validation of experimental results are presented in Refs. [16, 17].

The focus of our tests was a two-stream nozzle configuration, referred to as the plug20 nozzle, which integrates a

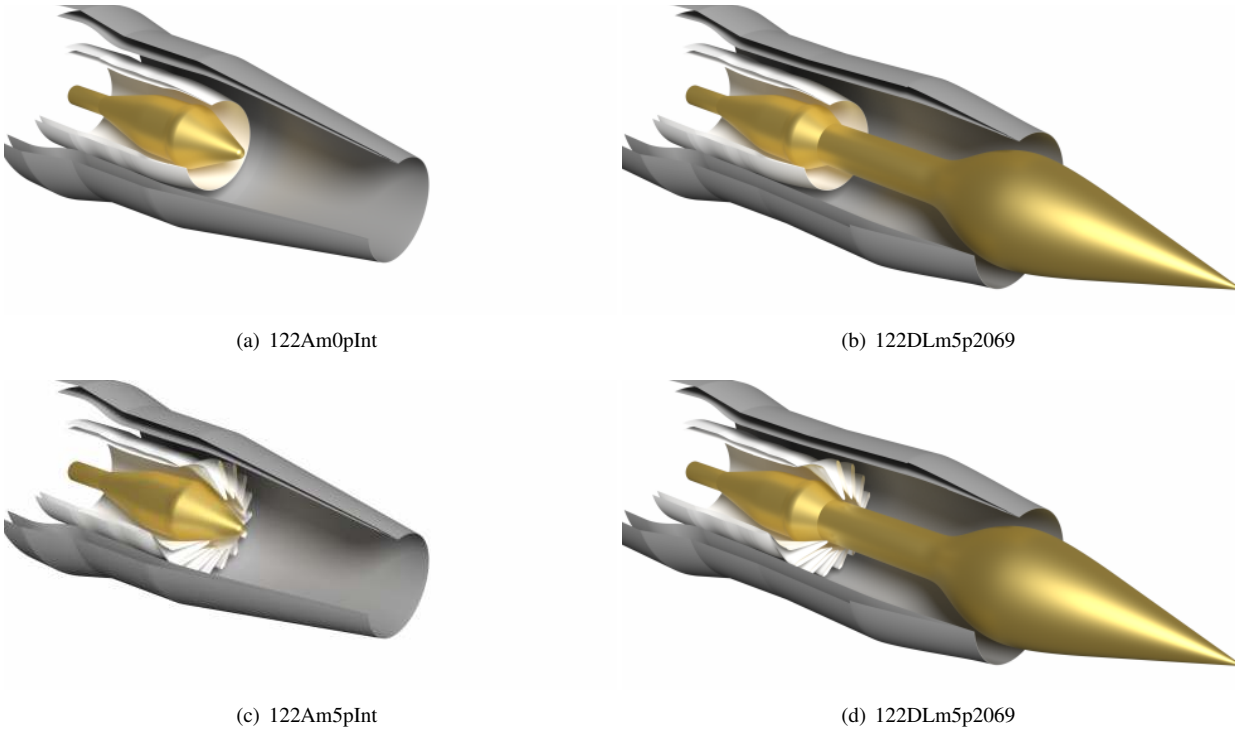

(a) 122Am0pInt (b) 122DLm5p2069

(c) 122Am5pInt (d) 122DLm5p2069

Fig. 1 Dual-stream, internally mixed plug20 nozzles used in this study: Internal plug nozzles with (a) axisymmetric splitter m0 (c) lobed mixer m5. External plug nozzle (b) with axisymmetric splitter m0 (d) lobed mixer m5. Renders were made by Timothy Sandstrom from NASA Ames using in-house developed tools.

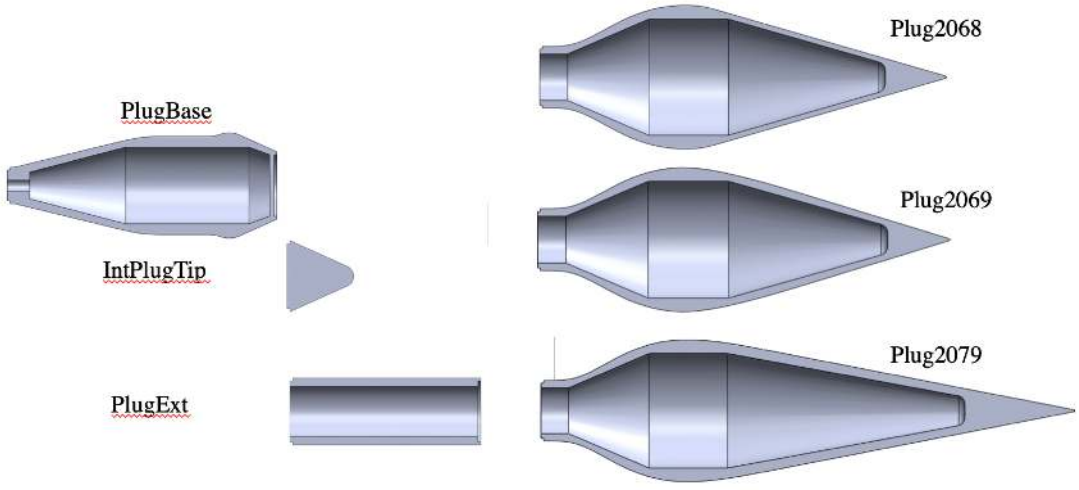

Fig. 2 Plug components: PlugBase (common), IntPlugTip (internal plug), short plug with shock (plug2068), short plug without shock (plug2069), long plug (p2079), PlugExt is used for long plug configuration only [14]

plug, an internal mixer, and the nozzle body. This configuration is bifurcated into two distinct setups: internal and external plug configurations. Figure 1(a-b) illustrates the differences between these configurations. Specifically, the internal plug setup employs nozzle 122A, whereas the external plug setup utilizes nozzle 122D, accompanied by several plug options (p2068, p2069, p2079) as shown in Figure 2. For the purposes of this paper, we focus primarily on

results from the p2069 plug, although it is worth mentioning that some experimental data pertains exclusively to the p2068 configuration. Notably, NASA CST's technical lead for jet noise James Bridges has confirmed that the noise differences between these configurations are minimal. The internal mixing is facilitated by two interchangeable mixers, as depicted in Figure 1. An additional feature available for the external configuration is an extension of the plug by 0.2m (PlugExt), leading to a nomenclature of 122DS for the shorter, non-extended version and 122DL for the extended version. Further details on the components of the plug20 nozzle are discussed extensively in several publications by Bridges et al.[2, 14, 18]. In this study, we examine two internal plug configurations (122Am0pInt, 122Am5pInt) and two external configurations (122DLm0p2069, 122DLm5p2069), chosen to simulate the operational conditions of a two-stream engine in commercial supersonic aircraft. Various set-points, defined by differing pressure and temperature ratios, are specified in Table1.

Table 1 Engine Cycle Matrix. Nozzle Pressure ratio (NPR) of core (C) and bypass (B) stream. Mach number of flight stream (MF). Mass flow rate (W).

Setpoint	M_{ref}	NPR_C	NTR_C	W_C [lbm/s]	NPR_B	NTR_B	W_B [lbm/s]	U_{jet} [m/s]
70	0.01	1.854	0.993		1.854	0.985		306
71	0.10	1.854	0.998		1.854	0.997		306
73	0.20	1.858	0.996		1.858	0.996		306
75	0.30	1.856	1.000		1.856	1.000		306
1180	0.02	1.807	2.905	2.63	1.801	1.202	11.53	507
1183	0.30	1.807	2.905	2.63	1.801	1.202	11.53	507
1200	0.02	1.997	3.253	2.99	1.993	1.199	12.50	597
1203	0.30	1.997	3.253	2.99	1.993	1.199	12.50	597

Table 2 Matrix of experimental and simulation data available for this study

Setpoint	DLm0p2069			DLm0p2069			DLm0p2069			DLm0p2069		
	PIV	FF	CFD	PIV	FF	CFD	PIV	FF	CFD	PIV	FF	CFD
70	✓	✓	✓	✗	✓	✓	✗	✓	✓	✓	✓	✓
71	✓	✓	✓	✗	✗	✗	✗	✗	✗	✗	✗	✗
73	✓	✓	✓	✗	✗	✗	✗	✗	✗	✗	✗	✗
75	✓	✓	✓	✗	✗	✓	✗	✗	✓	✗	✗	✓
1180	✗	✓	✓	✗	✓	✓	✗	✗	✓	✗	✓	✓
1183	✗	✓	✓	✗	✓	✓	✗	✓	✓	✗	✓	✓
1200	✓	✓	✓	✓	✓	✓	✗	✗	✓	✓	✓	✓
1203	✓	✓	✓	✓	✗	✓	✗	✓	✓	✓	✓	✓

III. Computational Methodology

The LAVA solver framework [19] is utilized for the computational study. LAVA offers flexible meshing options and was developed with the intent of modeling highly complex geometry and flow-fields. The framework supports Cartesian and curvilinear structured grids as well as unstructured arbitrary polyhedral meshes. For this work the compressible Navier-Stokes equations are solved using a finite-difference formulation applied to the curvilinear transformed system of equations in strong conservation law form using a 3rd order RK3-TVD time integration scheme [20]. Overset grid technology [21] is used to couple the solutions across different overlapping meshes. In this study, the structured curvilinear overlapping grid methodology is used with the WMLES approach. The curvilinear overset grids are generated utilizing the Pointwise^{TM} and Chimera Grid Tools (CGT) [22] software packages.

A. Low Dissipation Finite-Difference Method

High-order accurate low dissipation finite-difference schemes have been shown to be an accurate and efficient strategy for turbulence resolving simulations using LAVA [23–26] . A thorough study comparing several high-order finite difference methods on Cartesian grids within the LAVA framework was reported previously [27]. Results from this study indicated that high-order Weighted Essentially Non-Oscillatory (WENO) schemes [28] performed well in both resolution (Points-Per-Wavelength PPW), shock capturing, and robustness under harsh flow conditions. A natural extension of finite-difference WENO schemes to curvilinear grids are the high-order Weighted Compact Nonlinear Schemes (WCNS)[29]. The WCNS method, used for convective fluxes, involves a WENO or high-order interpolation (instead of reconstruction) of the left and right states to the half-grid points. This is followed by the evaluation of the numerical flux at these points using an approximate or exact Riemann solver, or a flux vector splitting scheme. Finally, a high-order central finite-difference operator is applied at the grid points, depending on the numerical fluxes at the half-grid points, either implicitly (compact) or explicitly. When applying finite-difference methods to the curvilinear equations in strong conservation law form, standard WENO finite-difference methods will not satisfy the Geometric Conservation Law (GCL) making it necessary to combine the WENO interpolation with high-order central-difference operators. It has been shown that free-stream preservation (i.e. the GCL condition) is satisfied up to machine precision provided that identical central difference operators are used for discretizing the metric terms as well as the fluxes [30]. An additional advantage of WCNS over WENO is the ability to use approximate Riemann solvers. Standard finite-difference WENO methods require the use of flux vector splitting methods for numerical flux evaluation. In this work, a modified version of the Roe numerical flux is used [31]. A consequence of using high-order central difference operators applied to numerical fluxes at the half grid points, which depend on high-order left and right state interpolations, is a much wider stencil required for the same order of accuracy compared to standard nodal finite-difference methods. To remove this pathology, high-order central difference operators using a combination of the numerical fluxes at the half grid points and the physical fluxes at the grid points have been developed [32, 33].This approach, denoted Hybrid Weighted Compact Nonlinear Scheme (HWCNS), allows for up to third/fourth-order accuracy using a five-point stencil by combining blended third- and fourth-order interpolation with a fourth-order hybrid central difference operator. The blending of an upwind biased and pure central variable reconstruction [34], has been generalized by the authors to variable interpolation. A detailed description of the implementation in LAVA is included in the appendix of Housman et al. [35].

In the current approach, the convective fluxes (and the metric-terms used within) are evaluated using a shock-sensor based blending between 3rd order WENO interpolation and 4th order central interpolation. Explicit RK3-TVD is used for physical time-integration with a CFL restriction of 1.25. Finally, a masking of the blended interpolation (of 50% 3rd order upwind and 50% 4th order central) is performed near overset fringe points to enhance robustness and reduce numerical artifacts which may occur near overset boundaries using low dissipation schemes. This is especially crucial for acoustic predictions as spurious oscillations at an overset interface can corrupt the far-field noise signal.

B. Wall-treatment for scale resolving simulation

The work presented in this paper uses an equilibrium wall model (no separate embedded grid necessary) with the analytic wall-function of Musker [36] to evaluate the wall-shear stress using the velocity at the matching location. Due to the low-Mach number character of the flow (and therefore lack of significant compressibility within the boundary layer), along with adiabatic treatment of the wall, the use of an analytic wall-function offers a computationally efficient alternative to solving the wall-normal ODEs derived from the thin boundary layer equations. Bocquet et al. (2012) [37], among others (see review by Larrson *et al.* [38]) have argued that for the flow regime being considered the analytic/algebraic wall-model and the ODE-based wall model are essentially identical in terms of accuracy.

The velocity input for the wall model is obtained from the second off-wall point [38], and the returned wall-shear stress serves as a viscous flux boundary condition for the PDE solved at the first off-wall point. This process includes appropriate tensor rotations to translate the data from local curvilinear coordinates to wall coordinates. For subgrid scale closure, the constant coefficient Sigma model [39] is used, with a model constant of 1.35. For more detailed information on WMLES and the applicability of an equilibrium wall model for non-equilibrium separated flows, refer to the reviews by Larsson et al. (2016) [38] and Bose Park (2018) [40]. For a more recent application of the wall-model within the LAVA solver and additional information on the numerical method see Ghate *et.al* [25, 26, 41] where the wall-model is applied to the NASA juncture flow experiment (JFM) and the NASA high speed Common Research Model (HS-CRM) for transonic flows.

C. Turbulent inflow generation

The noise produced by attached boundary layers, particularly those near a nozzle exit, is strongly influenced by 3D turbulent structures. These structures are crucial for the development of turbulent jet shear layers emanating from the nozzle, which in turn are key to accurate far-field acoustic predictions [11]. Capturing these complex flows requires sophisticated modeling techniques. Direct Numerical Simulation (DNS) and wall-resolved Large Eddy Simulation (LES) are typically necessary to fully resolve the intricate turbulent structures deep within the boundary layer [42]. However, the computational expense of wall-resolved LES for realistic Reynolds numbers, especially near the nozzle interior and exit, necessitates alternative approaches.

Wall-Modeled Large Eddy Simulation (WMLES) offers a viable solution by significantly reducing meshing requirements compared to wall-resolved LES [11, 43, 44]. In our approach, an equilibrium wall model is implemented in the nozzle interior, upstream of the nozzle exit. This section does not resolve turbulent fluctuations directly from the nozzle inflow to the wall-modeled section, thereby requiring the introduction of artificial turbulent fluctuations to foster the development of resolved turbulent structures within the boundary layer.

To initiate turbulence, tripping dots are employed on the geometries surface. Figure 27 illustrates an array of tripping dots utilized in this study. These dots are implemented using an immersed boundary penalty method, which introduces a source term to the momentum equations. The tripping dots are strategically placed only at the first point off the wall to minimize their impact on mass flow rate and boundary layer thickness. A staggered configuration of 144 equidistantly spaced tripping dots per trip row is used. This method has been found to have a minimal effect on the far-field noise spectra, demonstrating its effectiveness [8, 10].

Maintaining these small-scale turbulent structures effectively requires adequate mesh resolution, which can increase computational costs. It is crucial to determine the optimal placement of tripping dots upstream to balance accuracy and efficiency. Several tests have been conducted to evaluate and optimize the impact of tripping on far-field noise.

IV. Structured overset meshing approach for jet noise simulations

Structured overset curvilinear meshes were created utilizing Chimera Grid Tools [22] and Pointwise™software packages. These grids are particularly advantageous for aeroacoustic analysis of jet noise because they allow for the generation of high quality body-fitted grids. This capability is critical for capturing essential features such as nozzle boundary layers and shear layers, as well as for enabling local mesh refinement in the azimuthal direction at various streamwise and radial locations along the jet axis. Moreover, structured grid flow solvers are known for their efficiency, low memory requirements, and straightforward extension to high-order, low-dissipation finite-difference discretization. The use of overlapping grids not only simplifies the grid generation process, compared to structured multi-block abutting grids, but also results in higher-quality, less-skewed meshes.

The meshing strategy is divided into two main parts, as described below, adhering to our best practices for WMLES Jet Noise predictions derived from previous studies [9, 10]. The first part involves a near-wall mesh designed to meet the demands of WMLES simulations for wall-bounded flows. The second part focuses on a wake mesh, aimed at resolving the jet effectively while minimizing grid artifacts from large aspect ratio skewed cells. The near-wall mesh extends up to 0.5D, utilizing an overset approach to bridge these two regions. This approach aligns with the guidelines presented by Bogey et al. [45], Bres et al. [46, 47], and our previous hybrid RANS/LES [5, 7, 8] and WMLES [8] jet noise studies.

A. Wall-bounded near wall mesh region

The near-wall mesh region is essential for accurately capturing the boundary layer dynamics in the round jet, as depicted in Figure 4. This mesh is constructed by revolving a constant 2D mesh slice azimuthally with a fixed number of points. In contrast to Wall-Resolved Large-Eddy Simulations (WRLES) or Hybrid RANS/LES (HRLES), our Wall-Modeled Large-Eddy Simulation (WMLES) approach does not require the ultra-fine resolution of near-wall boundary layer gradients typically mandated by $\Delta_w^+ < 1$ wall resolutions. Thus, WMLES permits a more lenient specification in wall-normal meshing, which results in fewer points and more isotropic cells. Derived from precursor RANS simulations, the nozzle-exit boundary layer thickness informed our mesh design, targeting 10-20 points per boundary layer. This approach established a wall-normal spacing of $\Delta = 0.0015D$ for our final mesh resolution. Using an overset strategy, we compacted the near-wall resolution in the azimuthal direction around the mixer and nozzle lip regions, beginning 0.5D upstream of the lip. This strategy enhances fine-scale turbulent structures in the initial shear layer of the nozzle, while maintaining overall mesh costs at a reasonable level. Employing the overset method further,

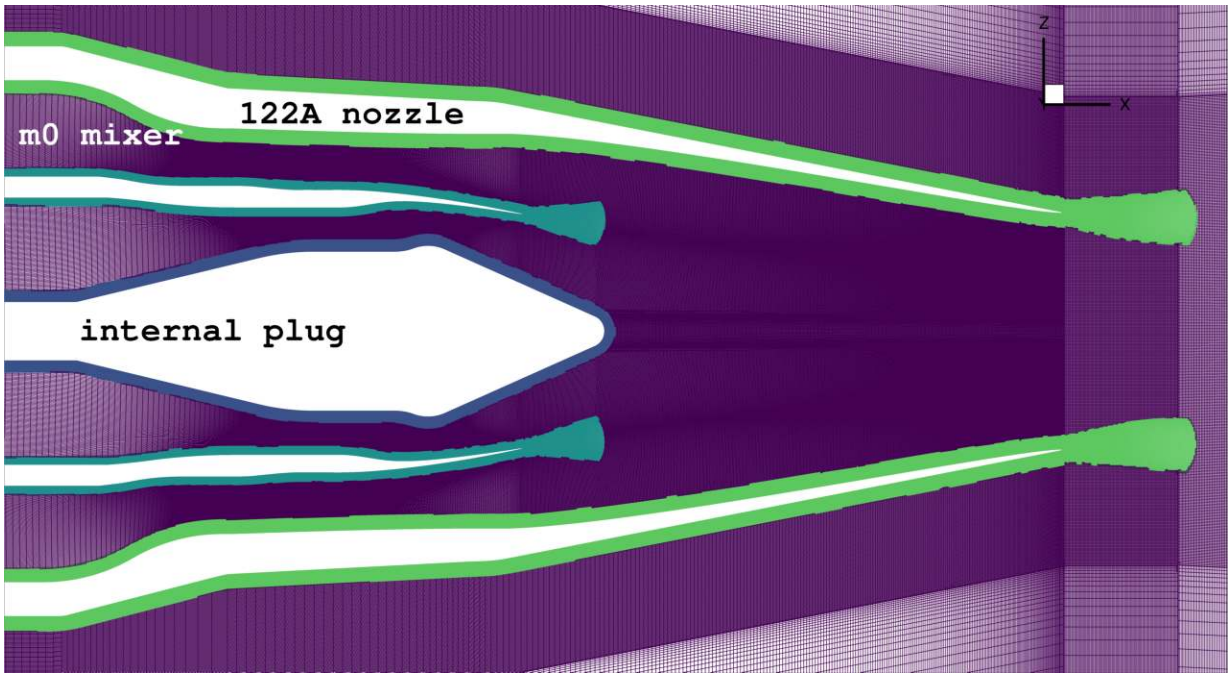

(a) 122ApIntm0

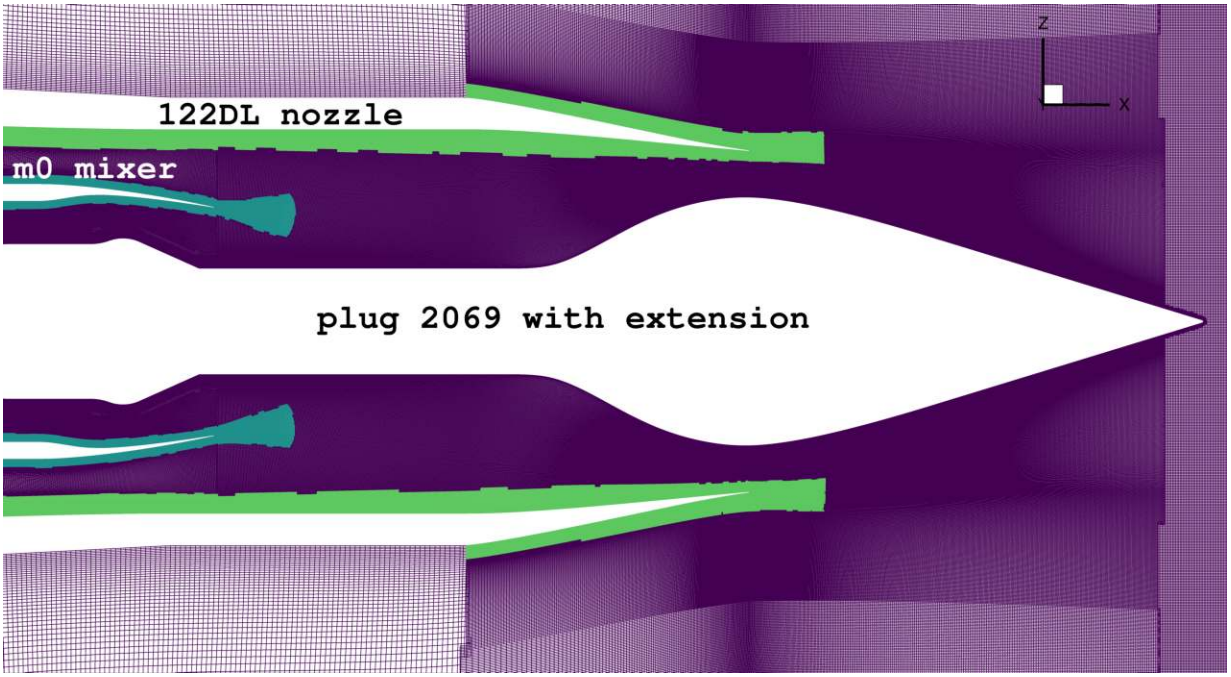

(b) 122DLp2069m0

Fig. 3 Near-wall body-fitted mesh with off-body block mesh for (a) internal plug case with m0 mixer (b) external plug with extension and m0 mixer.

we implemented a 2:1 coarsening in azimuthal resolution, culminating in a minimum of 361 points precisely at the nozzle inflow boundary layer.

One significant challenge in generating meshes for implicit time-marching schemes, such as the RK3 TVD scheme we use, lies in the local minima for the time-step. Governed by the Courant-Friedrichs-Lewy (CFL) condition, the

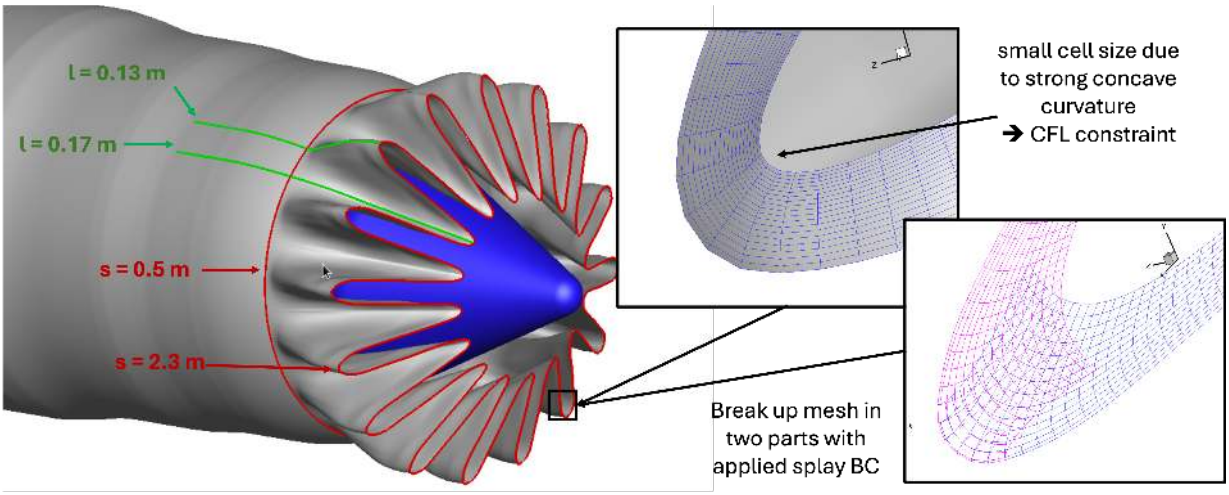

(a) Difference in geometric length scales for between m5 mixer tip and root

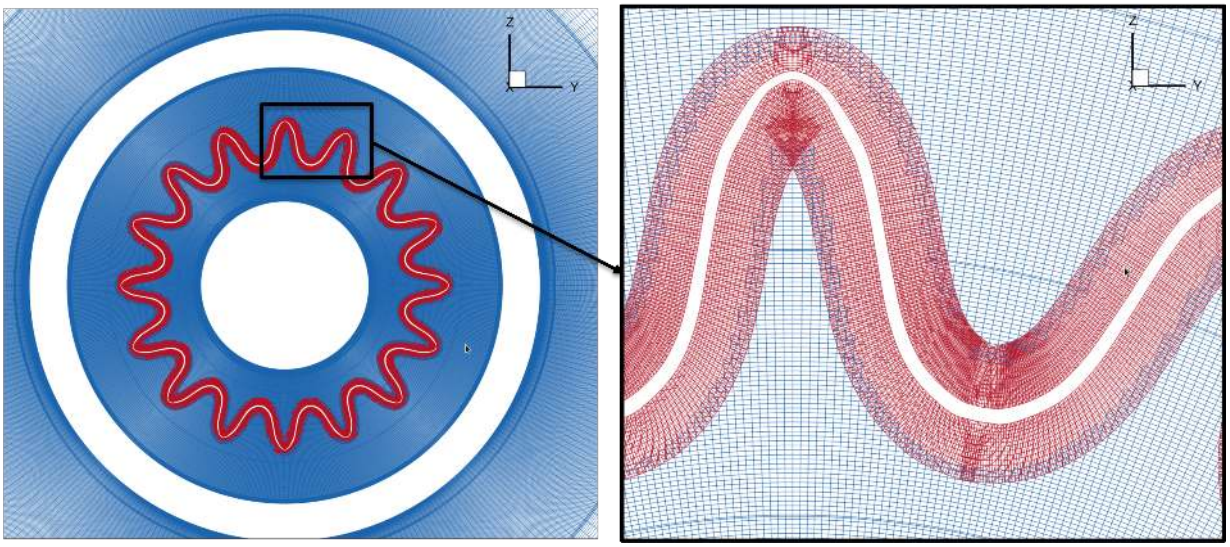

(b) slice through mesh at constant x location. Background mesh in blue and near-wall overset mesh in red

Fig. 4 Meshing strategy for lobed mixer m5 utilizing curvilinear overset meshing approaches.

time-step is determined by the characteristic velocity and length scale (e.g., cell size). Even if this results in a very localized minimum of the time-step, it impacts the global simulation costs, as the time-step is a global parameter based on the smallest necessary local time-step. Thus, generating the mesh requires meticulous attention, especially in convex mesh regions like those found in the valley of the m5 mixer lobes. Figure 4 highlights these challenges and the meshing approach employed for the lobed mixer. From previous studies, we know it is crucial to minimize overlapping meshes to reduce potential artificial numerical noise in areas with strong turbulent kinetic energy. Ideally, the entire near-wall mesh would encompass a single zone around the lobed mixer. However, as depicted in Figure 4(a), when comparing several length scales of the geometry around the mixer, the circumference at the tip is 4.6 times greater than at the base. Targeting an azimuthal mesh spacing of 0.002D would yield 7600 points at the tip versus 1600 points at the root. This discrepancy creates a dilemma where one must choose between accepting a smaller overall cell size at the root or a coarser azimuthal resolution at the tip, neither of which is viable. Additionally, it is exceedingly challenging to hyperbolically expand a volume mesh from a given surface in the mixer valley. Due to the pronounced convex corners, the cell size becomes inherently small away from the wall, as shown in Figure 4(a). To circumvent these issues, we utilized overset methods as much as necessary but as sparingly as possible. Initially, the mesh was segmented in the convex valley of the mixer with adequate overlap, and each volume was expanded separately. This strategy significantly

improved cell size away from the wall. In a subsequent step, we also applied a 2:1 coarsening in the azimuthal direction toward the mixer root to prevent the azimuthal spacings from becoming excessively small. The including of a lobed mixer increased the overall mesh count by around 15% and reduces the time-step size (increased simulation costs) by around 40% due to unavoidable small cell sizes.

This procedure has proven to be very manual and time-consuming, requiring adjustments for varying mixer designs, which could be a bottleneck when testing several mixer configurations within a short turnaround time. We have since investigated several different approaches, such as utilizing an immersed boundary method for the mixer. This alternative time and cost saving procedure is outlined in Section VII.

B. Jet potential core/wake mesh

The jet core/wake mesh, responsible for roughly two-thirds of the overall mesh costs, captures the turbulent structures emitted from the jet. In this study, we employed a square frustum approach, ensuring nearly isotropic cells with minimal stretching in the radial and streamwise directions. This is achieved by defining start and end values for the axis, along with side lengths at these points, and then stretching the mesh in the streamwise direction according to a pre-defined ratio until reaching a globally maximum spacing. Once this maximum is achieved, the streamwise spacing remains constant.

This automated approach can be easily adapted to various nozzle geometries, making it an efficient meshing strategy. It offers the additional benefit of maintaining nearly isotropic aspect ratio cells, which contrasts with traditional curvilinear methods that often result in varied mesh spacings farther from the nozzle centerline. Notably, it eliminates the singularities typically present at the centerline in conventional curvilinear jet meshes and avoids the complexities of overset topologies in the turbulent jet region. Table 3 details the spacings and parameters for the two square frustums used in mesh generation. This strategy yielded an overall mesh count for the combined near-wall mesh and the potential core/wake mesh of approximately 400 million grid points, depending on the configuration (see Table 4).

Table 3 Spacing's describing mesh in wake at different sections. Subscript lo and hi describe the lower and higher corner dimensions of the box for each section. Where x is the streamwise direction, R is the radial extend and Δ describes the "almost" uniform mesh spacing in all three coordinate directions. All spacings and locations are normalized with jet exit nozzle diameter D.

mesh prefix	x_{lo}	a_{lo}	Δ_{lo}	x_{hi}	a_{hi}	Δ_{hi}
frustum 1	0.0	1.5	0.0075	70.0	18.0	0.09
frustum 2	70.0	18.0	0.5000	5.5	26.0	1.00

Table 4 Representative mesh spacings at nozzle exit x=0.0: azimuthal number of points np_θ and number of mesh points of near wall mesh, plume and total mesh.

Configuration	$\Delta x/D$	$\Delta r/D$	$\Delta\theta/D$	np_θ	near-wall	plume	total
122Am0pInt	0.003	0.0015	0.002	1441	160M	240M	400M
122Am5pInt	0.003	0.0010	0.001	1441	220M	240M	460M
122DLm0p2069	0.003	0.0015	0.002	1441	168M	252M	420M
122DLm0p2069	0.003	0.0015	0.002	1441	228M	252M	480M

V. PART I: Application of Established Best Practices to Supersonic Jet Noise Configuration

In this initial part of the study, we apply aeroacoustic best practices established for canonical round jets by Stich et al.[8–10], Bres et al.[46, 47], and Bogey et al. [48] and others, to more complex supersonic nozzle configurations with internal mixing and plugs. These methodologies, which have been well-validated in simpler jet flows, are now challenged by the increased complexity of supersonic nozzles that feature intricate geometric variations and demanding flow conditions.

This section documents the outcomes of applying these traditional practices to advanced configurations, specifically highlighting how the methodologies adapted to and performed under these new conditions. We aim to detail where

these practices succeeded in maintaining their predictive accuracy and identifies areas where discrepancies between experimental results and simulations emerged. By mapping the performance of these established methodologies onto more complex scenarios, we aim to evaluate their robustness and identify potential modifications necessary for improved accuracy. The insights gained here will inform the more detailed investigative approaches discussed in Part II, which are designed to address and rectify the identified discrepancies. Additionally, more comprehensive post-processing has been conducted, including but not limited to two-point correlations, Spectral Proper Orthogonal Decomposition (SPOD), and other advanced analysis techniques. Details of these processes and their findings will be published in more detail in an upcoming journal paper.

A. Comparison to Experimental Data: Near-Field

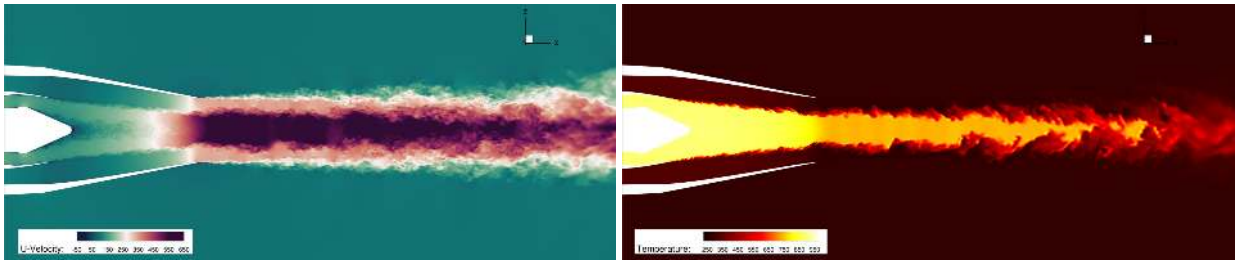

(a) SP1200 - 122Am0pInt

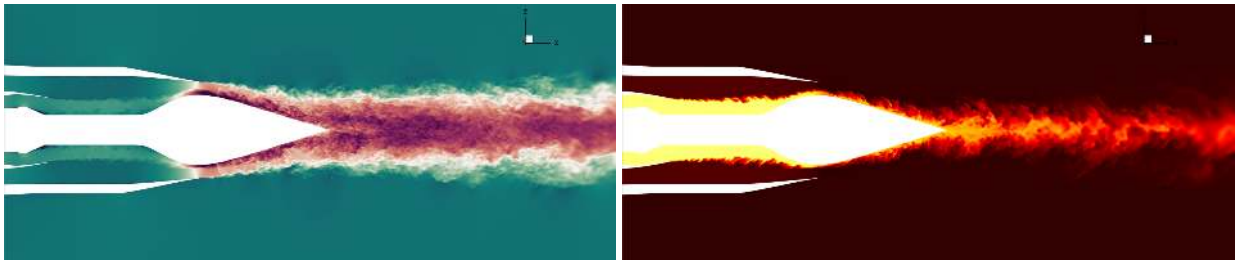

(b) SP1200 - 122DLm0pInt

Fig. 5 Instantaneous streamwise velocity (left) and temperature (right) for internally mixed configuration with a axisymmetric splitter m0 (a) internal plug and (b) external plug. Simulations were conducted for SP1200. Velocity displayed in m/s.

While near-field comparisons are not the primary focus of this study, which instead emphasizes differences in far-field acoustic measurements and simulations, we encourage readers to anticipate our upcoming journal publication. This forthcoming work will delve into detailed quantitative comparisons with near-field statistics, including centerline and lipline measurements of velocities and stresses. Additionally, the forthcoming paper aims to provide a deeper understanding of the flow dynamics influenced by various configurations, highlighting observed differences and addressing these.

This section aims to qualitatively demonstrate the differences among the four configurations and their respective impacts on the flow field. Moreover in this section we want to give a general understanding of the underlying flow features and how they are impacted by the different configurations. We then want to point out differences observed and try to address them in part II of this study in Section VI. Initially, we establish the effects of internal versus external plugs on the flow dynamics. Figure 5 illustrates the instantaneous streamwise velocity and temperature profiles for an internally mixed nozzle with an axisymmetric splitter plate, showcasing both internal (a) and external (b) plug configurations at set-point SP1200. A notable observation includes a decrease in centerline velocity for the external plug, alongside enhanced temperature mixing of the core and bypass streams at the nozzle exit, resulting in a cooler jet potential core. Additionally, we observe elongation in the turbulent structures within the mixer's shear layer at the nozzle exit due to the flow turning induced by the plug's curvature. A subtle shock structure approximately 1/6D downstream of the nozzle exit for the external plug configuration is visible in Figure 5(b), which aligns with experimental observations.

Figure 6 presents contour plots of vorticity gradient magnitude for the dual-stream 122DL nozzle with external plug

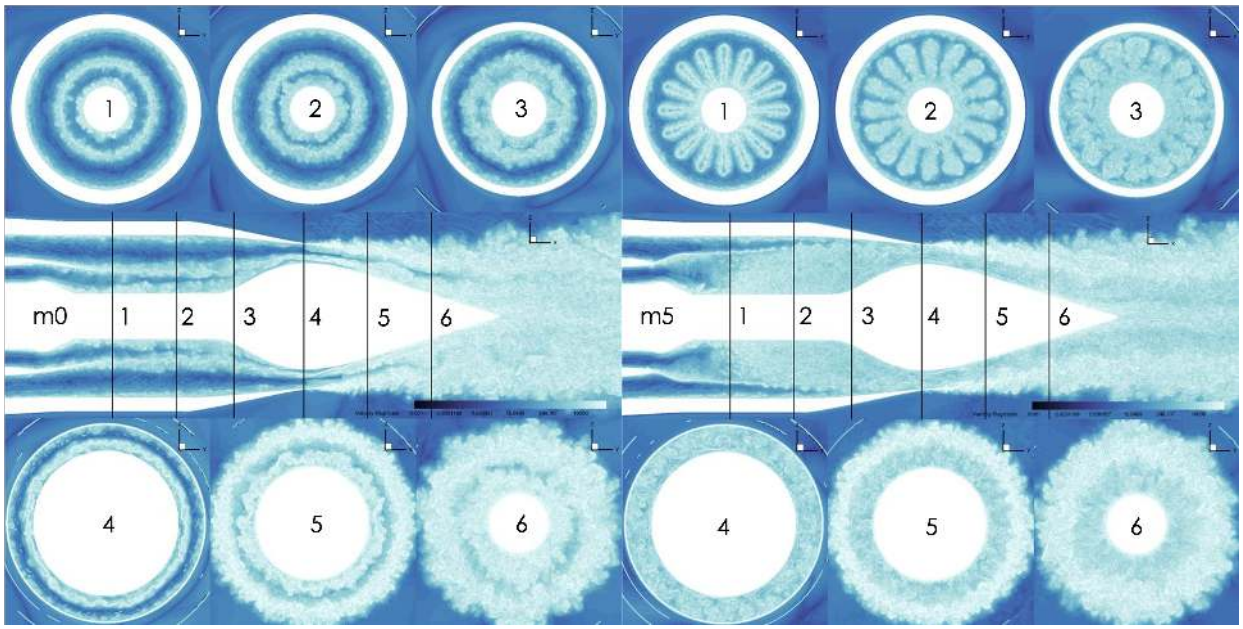

Fig. 6 Contours of Vorticity Gradient Magnitude for the Dual-Stream (122DL), External Plug (p2069) Configuration: This figure presents contour plots at various streamwise cuts, comparing the axisymmetric splitter (m0) on the left with the lobed mixer (m5) on the right for SP1200.

p2069. The comparison between an axisymmetric splitter plate m0 (left) and the corresponding lobed mixer m5 (right) illustrates the effective mixing induced by the lobed mixer. This configuration aims to ensure a thoroughly mixed plume at the nozzle exit, optimizing the process to enhance thrust while potentially reducing jet noise significantly [3]. The effects of this enhanced mixing are evident in the streamwise slices 1-4 of the figures, where the lobed mixer disrupts the distinct mixer shear-layer visible up to the nozzle exit in the axisymmetric case, resulting in an almost fully mixed flow at exit station 4.

We also seek to qualitatively compare mean-flow quantities between our WMLES LAVA simulations and experimental PIV data. While a comprehensive comparison including lipline and centerline statistics will be detailed in our upcoming journal paper, it's important to note that experimental data was available for three of the four configurations studied. Notably, the 122DLm0p2069 configuration was excluded from further experimental PIV analysis due to its pronounced noise characteristics and was deemed unfit for future applications. In our simulations, the axisymmetric nature of the configuration allowed for additional azimuthal averaging, achieving a smoother and more statistically converged solution. Figures 8 and 7 display the streamwise velocity and Reynolds-stress profiles from experimental PIV (left) and LAVA WMLES (right), highlighting the statistical challenges in the PIV dataset due to the absence of azimuthal averaging. Initial comparisons indicate symmetry in both stresses and velocities for the internal plug configuration (122A with pInt). However, the external p2069 plug case exhibits a markedly non-symmetric flow field attributed to plug deformation during the experiments for both cold (e.g., SP70) and hot (e.g., SP1200) setups, with more pronounced deformation observed under hot conditions due to thermal and gravitational effects. This deformation was not initially accounted for in our LES for part I of this study, but was incorporated in Section VI.A to assess its impact on noise and flow dynamics.

Further analysis reveals discrepancies in the length of the potential core between PIV and LES for the internally mixed 122Am0pInt configuration, as depicted in Figure 8(a), with LES predicting a significantly elongated potential core. Efforts to reconcile these differences have included modifications to internal geometries and additional computational studies, yet a definitive cause for this discrepancy remains elusive. Notably, we engaged in discussions with other researchers working on similar problems, who have observed comparable phenomena. Additionally, our own internal efforts employed a different numerical approach, independent of the one used in this study, which corroborated these findings. Despite these extensive efforts, the exact origins of the discrepancy have not been fully determined. Conversely, comparisons for the 122A5pInt configuration at SP1200 show excellent agreement between simulation and experiment, underscoring the complex interplay of factors influencing these outcomes.

Lastly, our examination of flight stream effects on the plume in configurations like SP1183 and SP1203, which

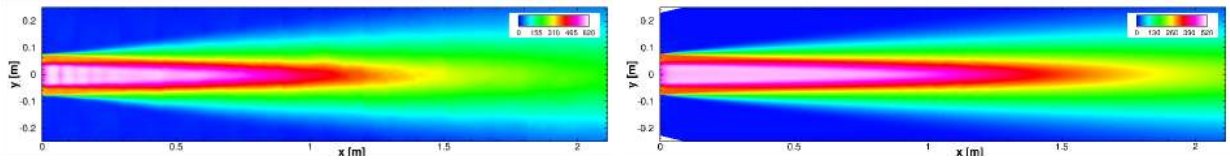

(a) UVelocity: SP1200 - 122Am0pInt PIV (left) LES (right)

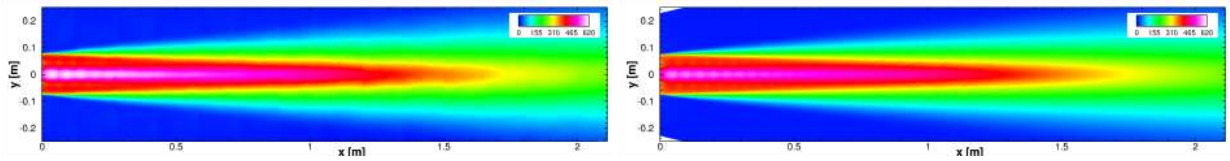

(b) UVelocity: SP1200 - 122Am5pInt PIV (left) LES (right)

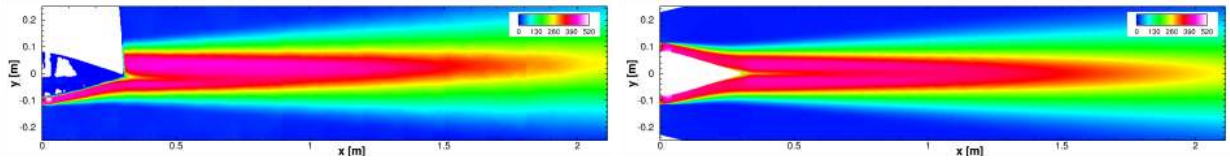

(c) UVelocity: SP1200 - 122DLm5p2069 PIV (left) LES (right)

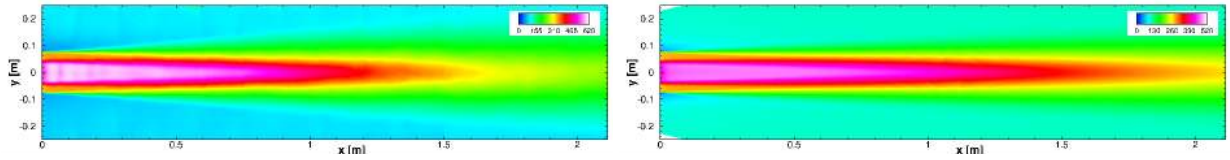

(d) UVelocity: SP1203 - 122Am0pInt PIV (left) LES (right)

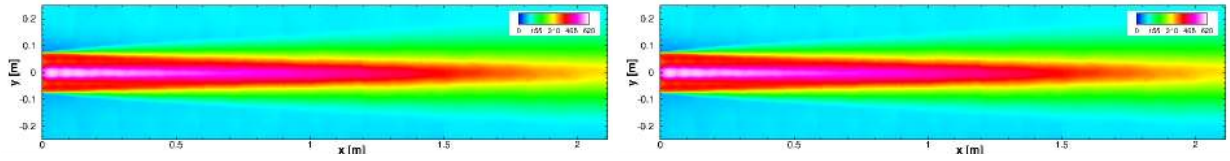

(e) UVelocity: SP1203 - 122Am5pInt PIV (left) LES (right)

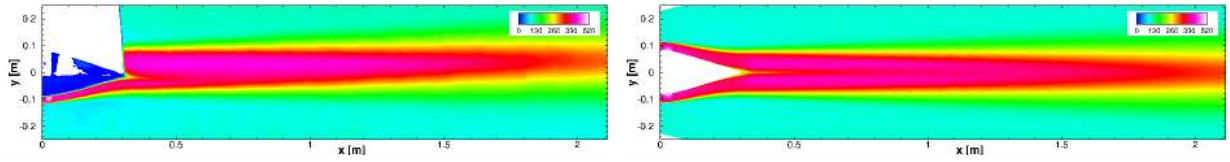

(f) UVelocity: SP1203 - 122DLm5p2069 PIV (left) LES (right)

Fig. 7 Mean axial velocity for experiment by Bridges [14] compared with LES data from LAVA simulations in baseline configuration. Velocity displayed in SI units of m/s.

introduce a co-flow of Mach 0.3, aligns with previous findings [10] that both PIV and LES observe an elongation of the potential core and a reduction in peak turbulent kinetic energy, consistent with the anticipated impacts of flight conditions on jet behavior.

B. Comparison to Experimental Data: Far-Field

The purpose of this section is to enhance our understanding of the far-field noise propagation using the permeable Ffowcs Williams-Hawkings (FWH) method within the LAVA framework [5, 49, 50]. This includes establishing

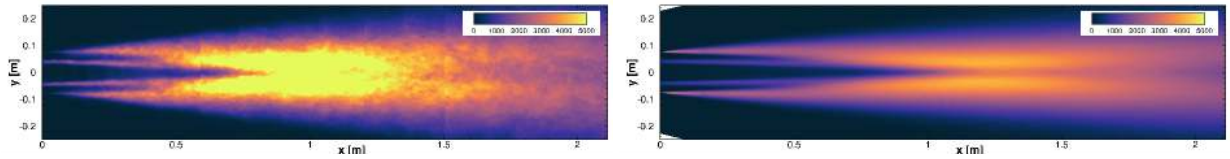

(a) u'u': SP1200 - 122Am0pInt PIV (left) LES (right)

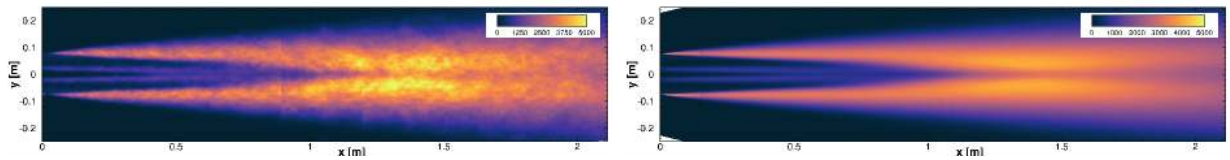

(b) u'u'y: SP1200 - 122Am5pInt PIV (left) LES (right)

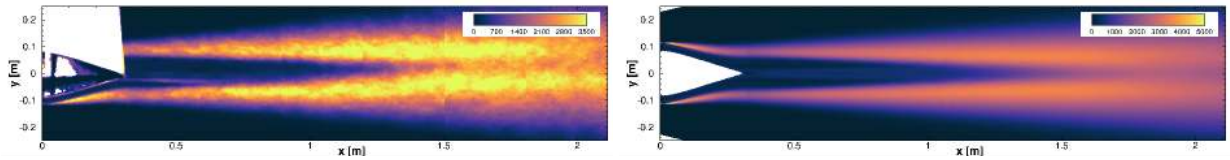

(c) u'u': SP1200 - 122DLm5p2069 PIV (left) LES (right)

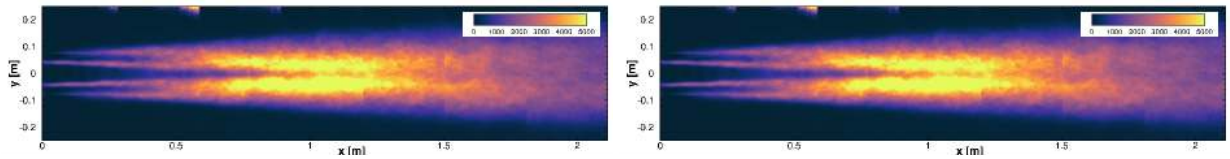

(d) u'u': SP1203 - 122Am0pInt PIV (left) LES (right)

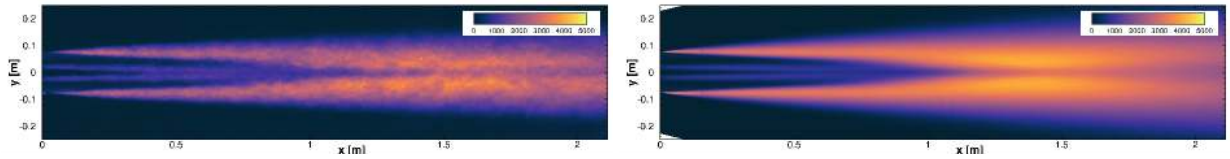

(e) u'u'y: SP1203 - 122Am5pInt PIV (left) LES (right)

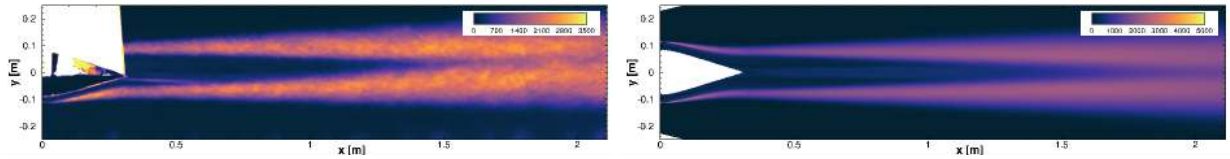

(f) u'u': SP1203 - 122DLm5p2069 PIV (left) LES (right)

Fig. 8 Mean axial velocity for experiment by Bridges [14] compared with LES data from LAVA simulations in baseline configuration.

best-practice guidelines applicable to more complex scenarios. A critical aspect noted is that the positioning of the FWH surface significantly influences the accuracy of jet noise simulations. Although there is no consensus in the literature regarding the optimal placement of the FWH surface relative to complex geometries and noise sources, various parametric studies have assessed the sensitivity of far-field noise predictions to the choice of FWH surface [42, 46, 47, 51–53].

Selecting an appropriate FWH surface is generally contingent on factors such as mesh resolution and the numerical scheme employed. There is a necessary balance between positioning the FWH surface close enough to the jet to capture all pertinent noise sources and maintaining sufficient distance to avoid spurious contributions from hydrodynamic

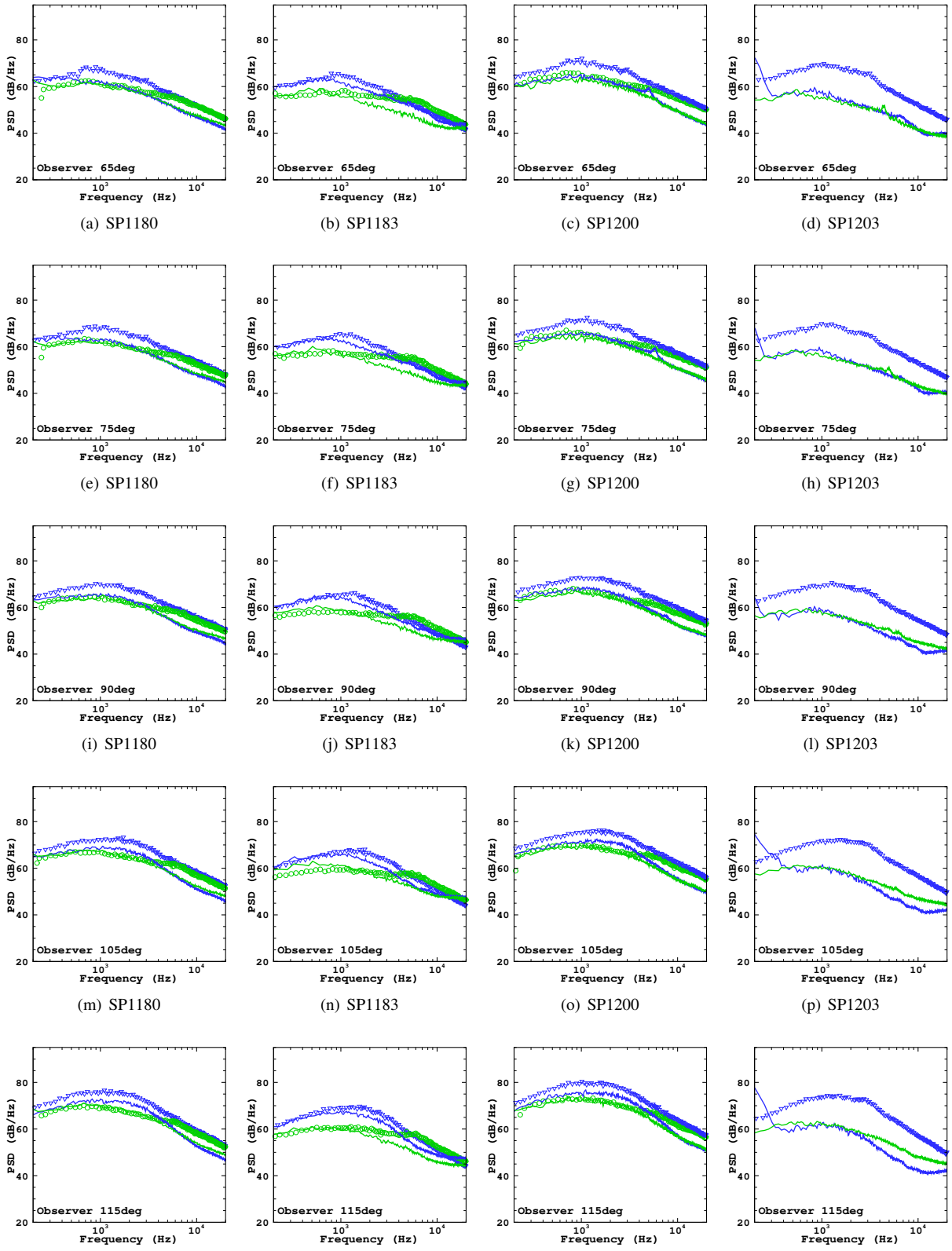

(a) SP1180 (b) SP1183 (c) SP1200 (d) SP1203

(e) SP1180 (f) SP1183 (g) SP1200 (h) SP1203

(i) SP1180 (j) SP1183 (k) SP1200 (l) SP1203

(m) SP1180 (n) SP1183 (o) SP1200 (p) SP1203

(q) SP1180 (r) SP1183 (s) SP1200 (t) SP1203

Fig. 9 Noise spectra at 100D from LAVA-WMLES simulations compared with experimental results by Bridges et al. (○ ▽) for the internal plug and mixer configuration 122AmXpInt. The figure shows results for both axisymmetric (——) and lobed (——) mixers. See Table ?? for availability of experimental data.

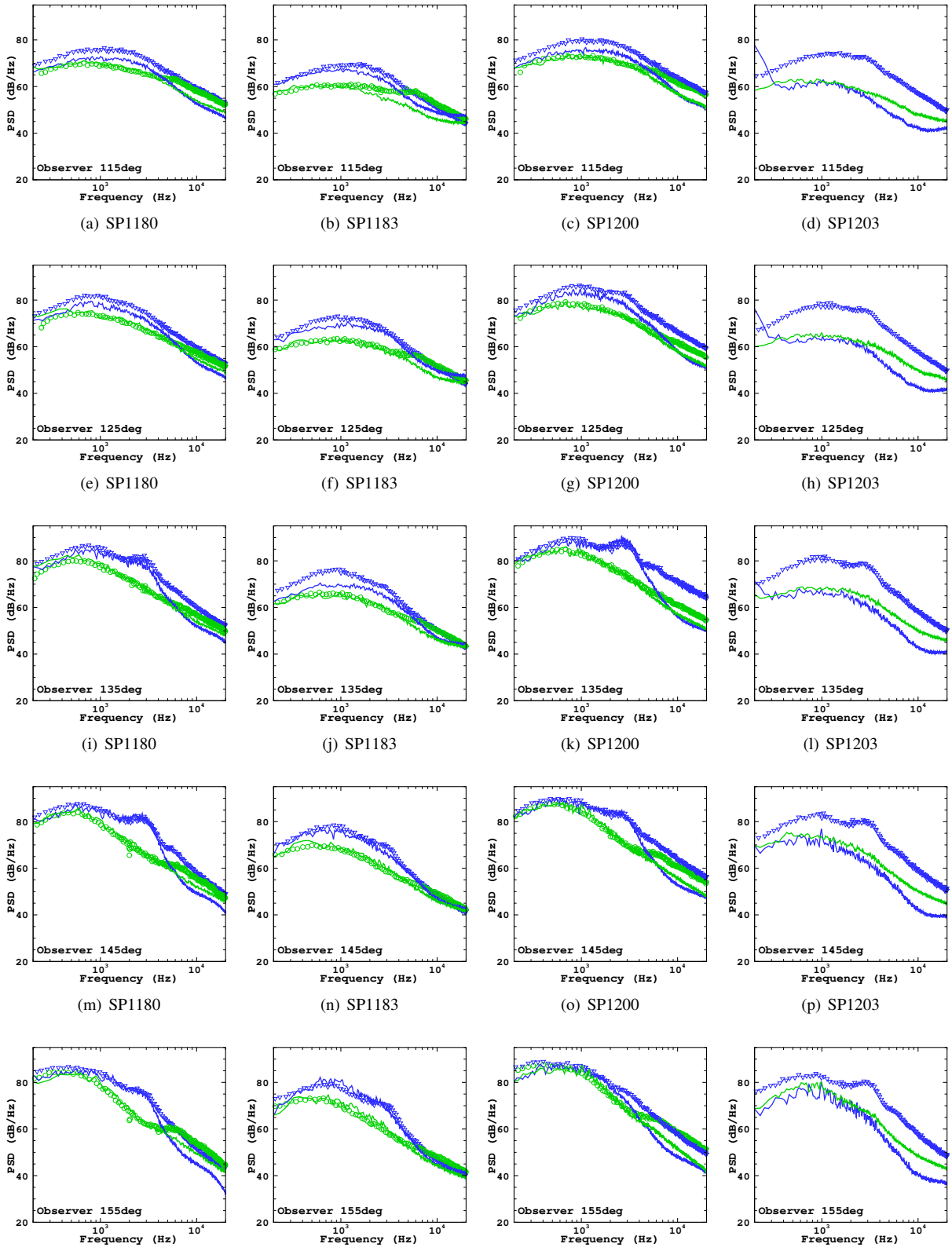

(a) SP1180 (b) SP1183 (c) SP1200 (d) SP1203

(e) SP1180 (f) SP1183 (g) SP1200 (h) SP1203

(i) SP1180 (j) SP1183 (k) SP1200 (l) SP1203

(m) SP1180 (n) SP1183 (o) SP1200 (p) SP1203

(q) SP1180 (r) SP1183 (s) SP1200 (t) SP1203

Fig. 10 Noise spectra at 100D from LAVA-WMLES simulations compared with experimental results by Bridges et al. (○ ▽) for the internal plug and mixer configuration 122AmXpInt. The figure shows results for both axisymmetric (——) and lobed (——) mixers. See Table ?? for availability of experimental data.

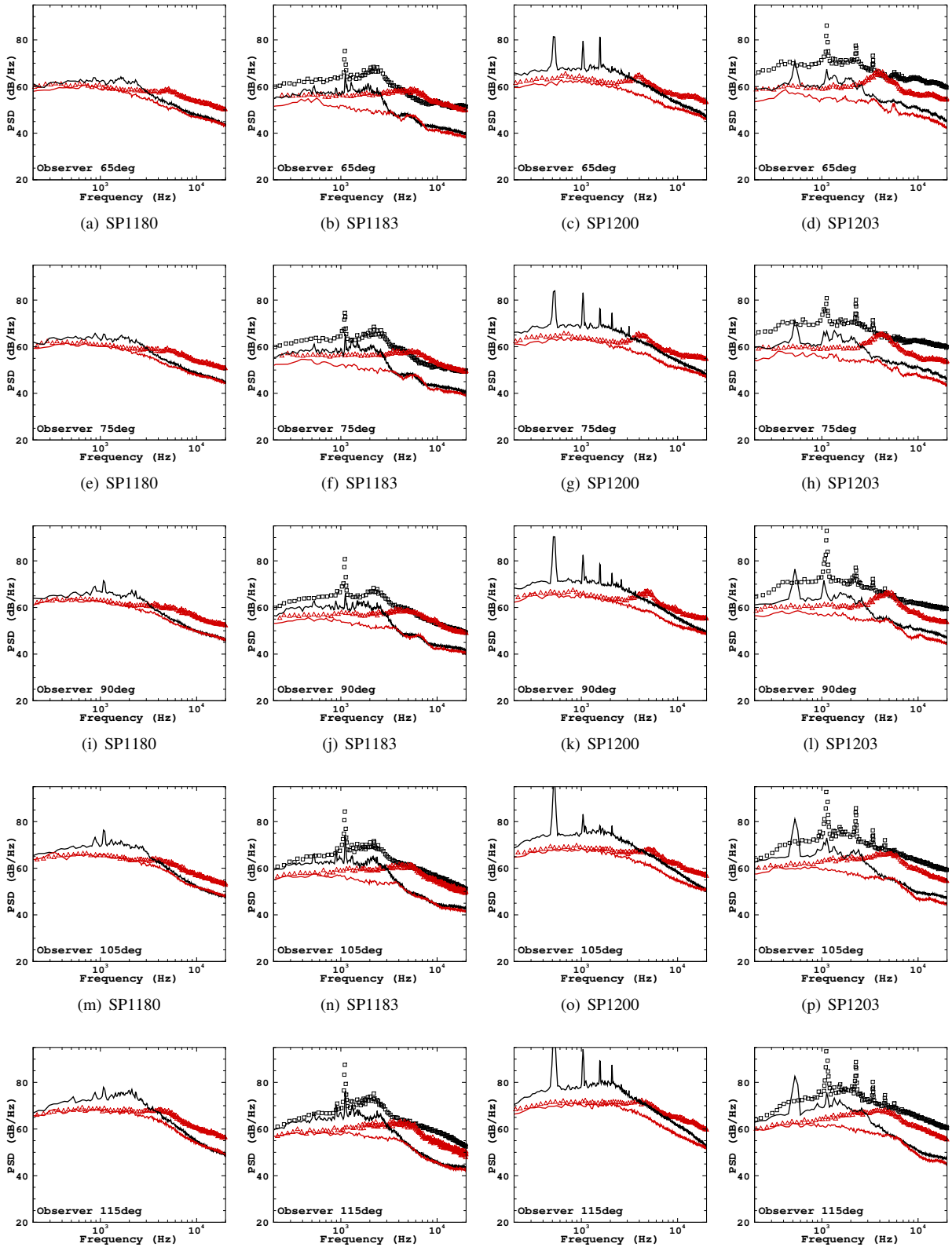

(a) SP1180 (b) SP1183 (c) SP1200 (d) SP1203

(e) SP1180 (f) SP1183 (g) SP1200 (h) SP1203

(i) SP1180 (j) SP1183 (k) SP1200 (l) SP1203

(m) SP1180 (n) SP1183 (o) SP1200 (p) SP1203

(q) SP1180 (r) SP1183 (s) SP1200 (t) SP1203

Fig. 11 Noise spectra at 100D from LAVA-WMLES simulations compared with experimental results by Bridges et al. (□ ▽) for the external plug and mixer configuration 122DLmXp2069. The figure shows results for both axisymmetric (——) and lobed (——) mixers. See Table ?? for availability of experimental data.

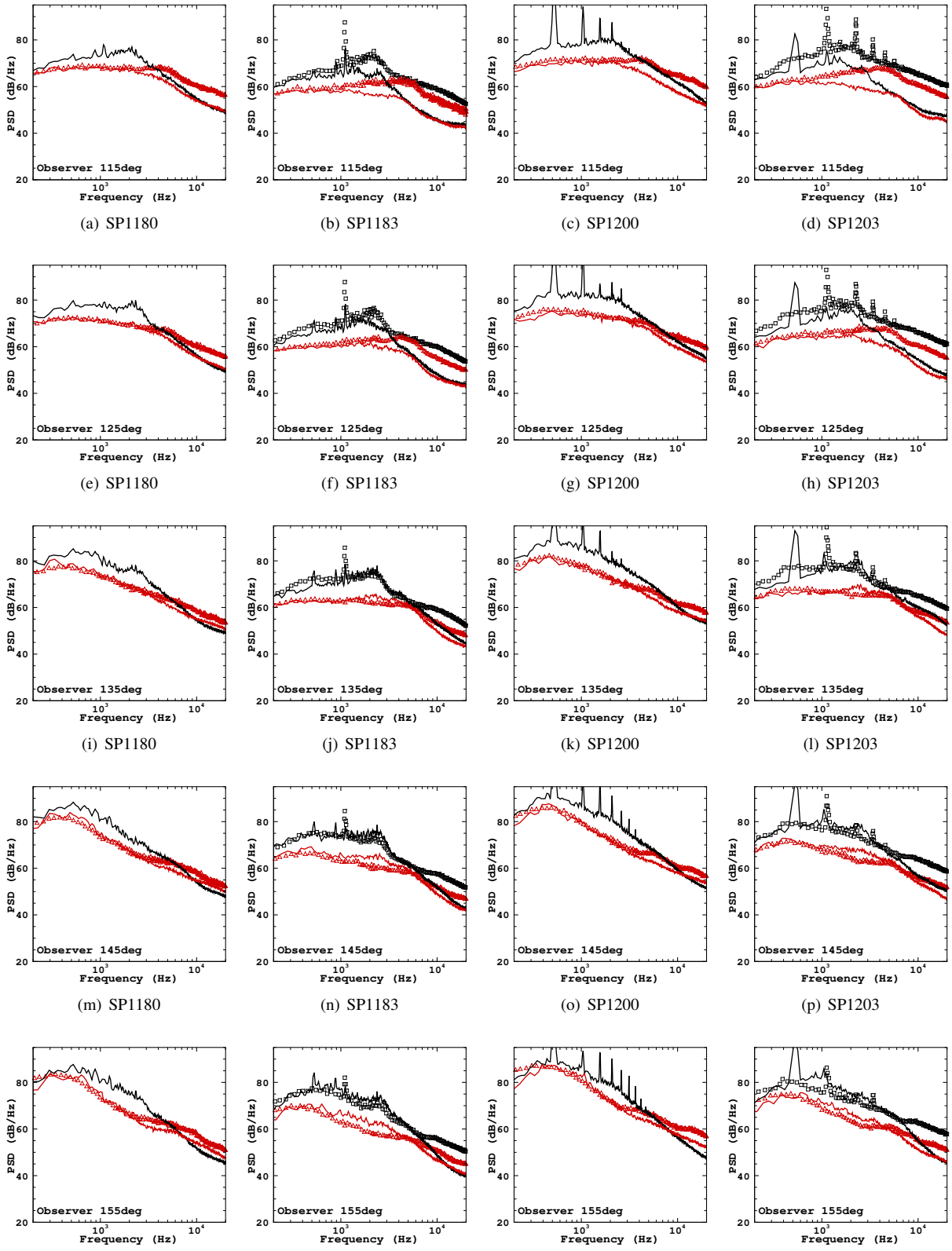

(a) SP1180 (b) SP1183 (c) SP1200 (d) SP1203

(e) SP1180 (f) SP1183 (g) SP1200 (h) SP1203

(i) SP1180 (j) SP1183 (k) SP1200 (l) SP1203

(m) SP1180 (n) SP1183 (o) SP1200 (p) SP1203

(q) SP1180 (r) SP1183 (s) SP1200 (t) SP1203

Fig. 12 Noise spectra at 100D from LAVA-WMLES simulations compared with experimental results by Bridges et al. (□ ▽) for the external plug and mixer configuration 122DLmXp2069. The figure shows results for both axisymmetric (——) and lobed (——) mixers. See Table ?? for availability of experimental data.

fluctuations crossing the surface. These spurious contributions are often due to the neglect of the volume integral of the quadrupole term in the FWH formulation, which can be somewhat mitigated by phase-averaging at the triangulation end-caps [54].

The frequency-domain permeable surface FWH equations used in LAVA align with those detailed by Lockhard [55] and are equivalent to those used by Bres et al. [11, 46], with a notable modification where the density perturbation is substituted with pressure perturbation, $\rho' := \rho_\infty + p'/c_\infty^2$, as suggested by Spalart et al. [56]. In constructing the FWH surface, we adhered to best practices from Bres et al. [46] and Mendez et al. [57], modifying them for in-flight effects as delineated by Stich et al. [10]. An in-depth analysis comparing end-cap averaging between $25D_j$ and $30D_j$ was conducted to eliminate spurious contributions from hydrodynamic pressure fluctuations, contrasting this with an open FWH surface configuration where both ends extend across the entire domain [5].

For the far-field propagation analyses, we utilized between 400CTU and 2000CTU based on the jet centerline velocity and nozzle exit diameter, following methodologies outlined in [11, 46]. The total time sample is segmented into 5-15 windows with 50 percent overlap, where a Hanning filter is applied to time-domain FWH integrands after removing the mean, followed by the Fast Fourier Transform (FFT) to shift the integrands into the frequency domain. This windowing process effectively reduces spurious noise at low frequencies, crucial for quieter sideline angles ($\Phi < 120°$). After completing the FFT, frequency-domain FWH surface integrals are evaluated for each observer location to compute the acoustic pressure p'. During PSD calculations, a correction factor of $\sqrt{8/3}$ compensates for the energy lost due to windowing. The PSD is then averaged across 72 observers to leverage symmetries, and the results are averaged over all windows. The final spectrum is subsequently compared to experimental data collected over a significantly longer time-window.

To ensure a consistent comparison of far-field noise spectra between the different configurations, identical FWH surface triangulations were employed. The triangulation adheres closely to the external nozzle shape with a consistent offset, flaring radially at $x/D_j = 0$ starting at $y/D_j = 0.8$ with a slope of 0.14. The numerical scheme requires approximately 8 points per wavelength to adequately resolve acoustic waves, setting the maximum resolvable Strouhal number at approximately $St_{lim} = D/(8 \cdot vol^{(1/3)} \cdot Ma)$ to be around 4. However, practical assessments have shown that accurate predictions can still be achieved above this theoretical limit.

In this analysis, our objective is to establish baseline results using standard best practices and identify any discrepancies in the noise spectra. These discrepancies will be thoroughly investigated in Part II of this study, where we will attempt modifications to the operational setup and computational models in an effort to influence and potentially improve the predicted noise spectra.

Power Spectral Density (PSD) profiles for 10 different observer angles located 100D from the jet exit are depicted in Figures 9 to 12, spanning four distinct flow conditions as listed in Table 1. Each column in these figures corresponds to one of the four specified set points (SPs). It should be noted that not all LES cases have corresponding experimental data for comparison. Some configurations exhibited significant howling noise during experimental tests and were therefore excluded from further consideration. To enhance clarity in visualization, results for internal plug configurations (122AmXpInt) and external plug configurations (122DLmXp2069) are presented in separate plots. In these plots, symbols denote experimental data, while lines represent LES simulation results. The data from each run are color-coded as follows: 122Am0pInt (▽——), 122Am5pInt (○——), 122DLm0p2069 (□——), and 122DLm5p2069 (▽——). It is important to highlight that the simulation results for the external plug configurations used the p2069 mixer, whereas the experimental data utilized a slightly different mixer configuration, p2068. According to internal communications with the experimental team, the noise differences between these two mixer configurations are minimal.
In this study, we do not aim to provide a detailed analysis of all noise results. Instead, our focus is on areas where significant discrepancies between simulations and experiments have been observed. By pinpointing these discrepancies, we seek to identify potential underlying causes and guide future modifications to improve the accuracy of our noise predictions. The key issues we want to highlight are:

a) Under-prediction of PSD at lower observer angles for axisymmetric m0 mixer: For the axisymmetric mixer configuration m0 under set-point SP1180, we have identified a notable difference in noise predictions at lower observer angles, up to 120 degrees. Notably, starting from 50 degrees, the results from the lobed mixer m5 and the axisymmetric mixer m0 become consistent, showing no significant differences in low-frequency noise between the two simulations. However, experimental results indicate a considerable disparity of several dB for frequencies up to 5000Hz. We have undertaken several methodological and geometric modifications to address these differences. These include adjustments to mesh resolution, refinement of the turbulent boundary layer, changes in numerical schemes, as well as alterations to the geometric setup such as the length of the mixer and plug, and breaking of symmetry. Despite these efforts, the

axisymmetric mixer consistently underperforms in capturing the lower frequency noise at angles less than 50 degrees compared to experimental observations. As observer angles increase beyond 120 degrees, the m0 results begin to diverge from the lobed mixer outcomes, aligning closely with experimental data and even capturing the characteristic hump in the frequency spectrum around 3000Hz. This alignment underscores the need for a more nuanced understanding of how geometric and numerical changes impact noise predictions at different observer angles.

b) Lack of high-frequency hump in m5 mixer results : Across all set-points, the results for the lobed mixer m5 align well with experimental outcomes in low to mid-frequencies, showcasing the effectiveness of this configuration in capturing the essential noise characteristics. However, for higher observer angles, both simulations and experiments exhibit a hump in the frequency spectrum, a feature that our LES has consistently failed to predict. The absence of this hump in LES results suggests potential limitations in our current modeling approach or numerical setup. To address this, further investigations are planned to explore the conditions under which this hump occurs and to identify potential modifications that could enable the LES to accurately predict this phenomenon. These explorations and potential solutions will be discussed in greater detail in Section VI.B, where we will examine boundary conditions and other factors that may influence the accuracy of high-frequency noise predictions.

The limitations previously discussed become particularly pronounced in the analysis of directivity and far-field spectral plots, as well as in the corresponding difference plots, presented in Figures 13 to 16. In these figures, the far-field noise is graphically represented for polar angles ranging from 55° to 165°, in increments of $\Delta\Theta = 5°$. The frequency is plotted along the x-axis, with the polar angle on the y-axis, and the power spectral density (PSD) values are displayed on the positive z-axis. To streamline the data presentation and reduce complexity, the PSD values are filtered through third octave bands. This processing involves integrating raw PSD values over the extent of each band, normalizing by the frequency band interval, and converting these values into decibels. The third octave center frequencies span from 200 Hz to 20,000 Hz. Experimental data is visualized using an opaque white mesh pattern. The difference between the experimental PSD and the simulation results for each octave band is highlighted in Subfigures (e)-(f). A black contour line, representing a ±2dB variance, delineates the areas where discrepancies between the experimental and simulation data are most pronounced. Notably, the m5 mixer data exhibits a consistent 5dB difference at higher frequencies across all angles, as shown in examples like Figure 13(f-g). In contrast, significant discrepancies for the m0 mixer are more apparent at upstream angles, as illustrated in Figure 15(e).

This persistent under-prediction of noise at certain conditions, discussed in detail by Gao Jun Wu in his Stanford thesis, has also been corroborated by current Stanford student Olivia Martin, who is actively researching plug20 nozzle configurations. These observations highlight the issue as a widespread challenge within the field, emphasizing the need for further investigation and potentially innovative solutions.

VI. PART II: Investigative Approaches to Resolve Discrepancies in Supersonic Jet Noise Prediction

In this second part of our study, we delve deeper into the intricate and unexpected challenges that surfaced when applying established aeroacoustic best practices, previously detailed in publications by Stich et al. [8–10], to the supersonic nozzle configuration. Initial findings highlighted significant discrepancies between experimental data and simulation outputs as described in section V, prompting a thorough investigation into the underlying causes and potential solutions. This section documents our multifaceted approach to resolving these discrepancies through a series of investigative measures.

We explore a range of geometric modifications designed to more accurately mimic real-world conditions and their impacts on noise generation. This includes adjusting the "droop" of the plug, caused by gravity and thermal effects, and incorporating an internal resonance in the mixer, aimed at altering the acoustic properties of the nozzle. Additionally, we experiment with variations in the flow physics, such as manipulating the boundary layer characteristics within the nozzle, which are critical to the accuracy of noise predictions.

We also performed a rigorous mesh refinement study as well as numerical study. We enhance the resolution and complexity of our meshes within critical regions of the nozzle to capture more detailed flow features in order to to assure we are significantly resolving our mesh. Each of these strategies—geometric, physical, and numerical—is meticulously tested and evaluated to discern their individual and collective impacts on the simulation results.

It is important to note that this investigation is ongoing, and additional findings will be detailed in an accompanying

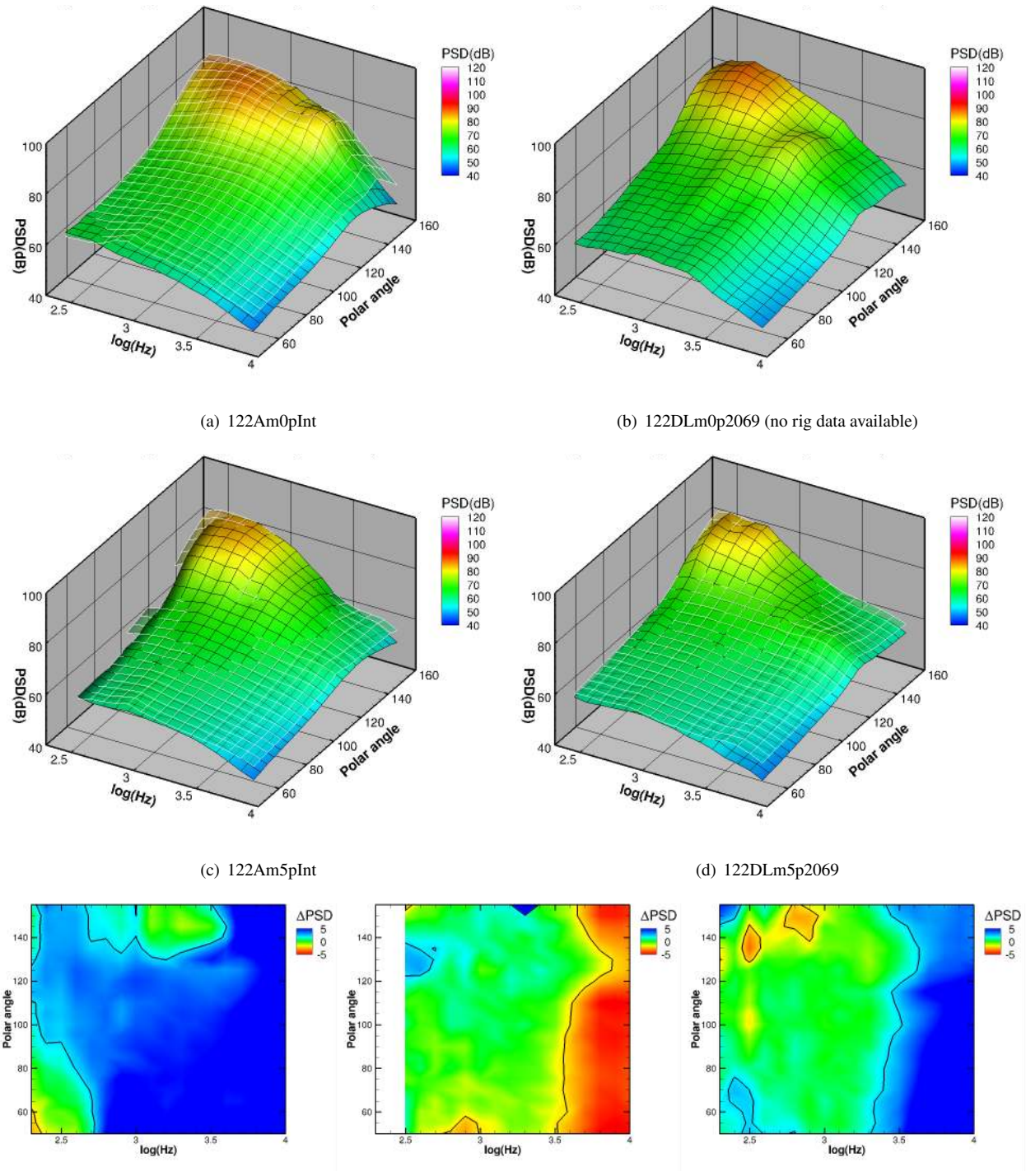

(a) 122Am0pInt

(b) 122DLm0p2069 (no rig data available)

(c) 122Am5pInt

(d) 122DLm5p2069

(e) 122Am0pInt

(f) 122Am5pInt

(g) 122DLm5p2069

Fig. 13 SP1180 [M_{ref}=0.02 ; NPR_C=1.807 ; NTR_C=2.905 ; NPR_B=1.801 ; NTR_B=1.202](a)-(d) Far-field spectra directivity comparison between WMLES LAVA data and rig data from [14]. The solid surfaces with black mesh represent WMLES data, while transparent surfaces with white mesh depict rig data. Panels (e)-(g) illustrate the differences between WMLES and rig data, with black contour lines representing ±2dB levels. Note: The LES data were generated for the p2069 plug, whereas experimental data were available only for the p2068 plug. This difference is expected to result in only minor discrepancies.

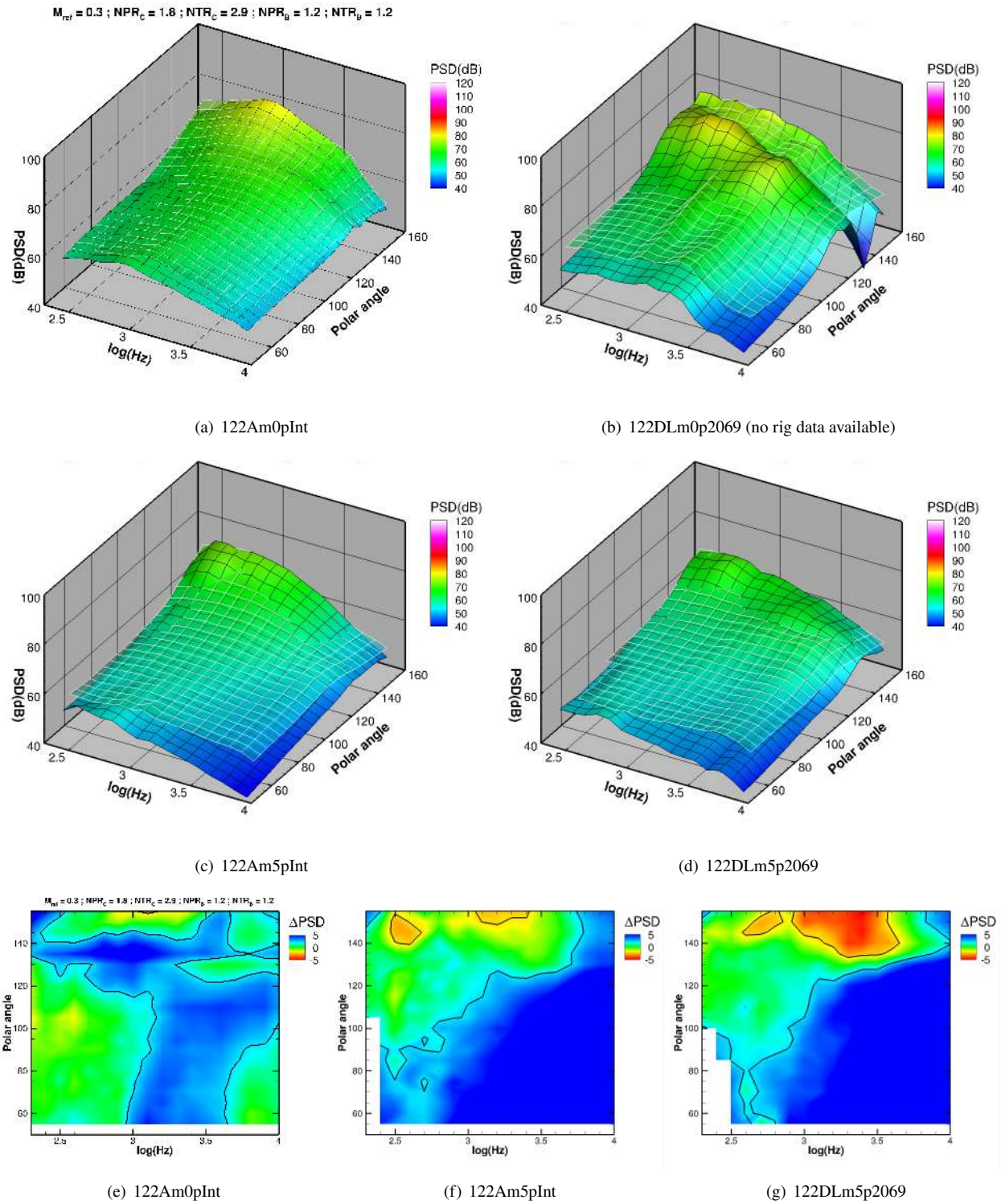

(a) 122Am0pInt

(b) 122DLm0p2069 (no rig data available)

(c) 122Am5pInt

(d) 122DLm5p2069

(e) 122Am0pInt

(f) 122Am5pInt

(g) 122DLm5p2069

Fig. 14 SP1183 [M_{ref}=0.3 ; NPR_C=1.807 ; NTR_C=2.905 ; NPR_B=1.801 ; NTR_B=1.202]. (a)-(d) Far-field spectra directivity comparison between WMLES LAVA data and rig data from [14]. The solid surfaces with black mesh represent WMLES data, while transparent surfaces with white mesh depict rig data. Panels (e)-(g) illustrate the differences between WMLES and rig data, with black contour lines representing ±2dB levels. Note: The LES data were generated for the p2069 plug, whereas experimental data were available only for the p2068 plug. This difference is expected to result in only minor discrepancies.

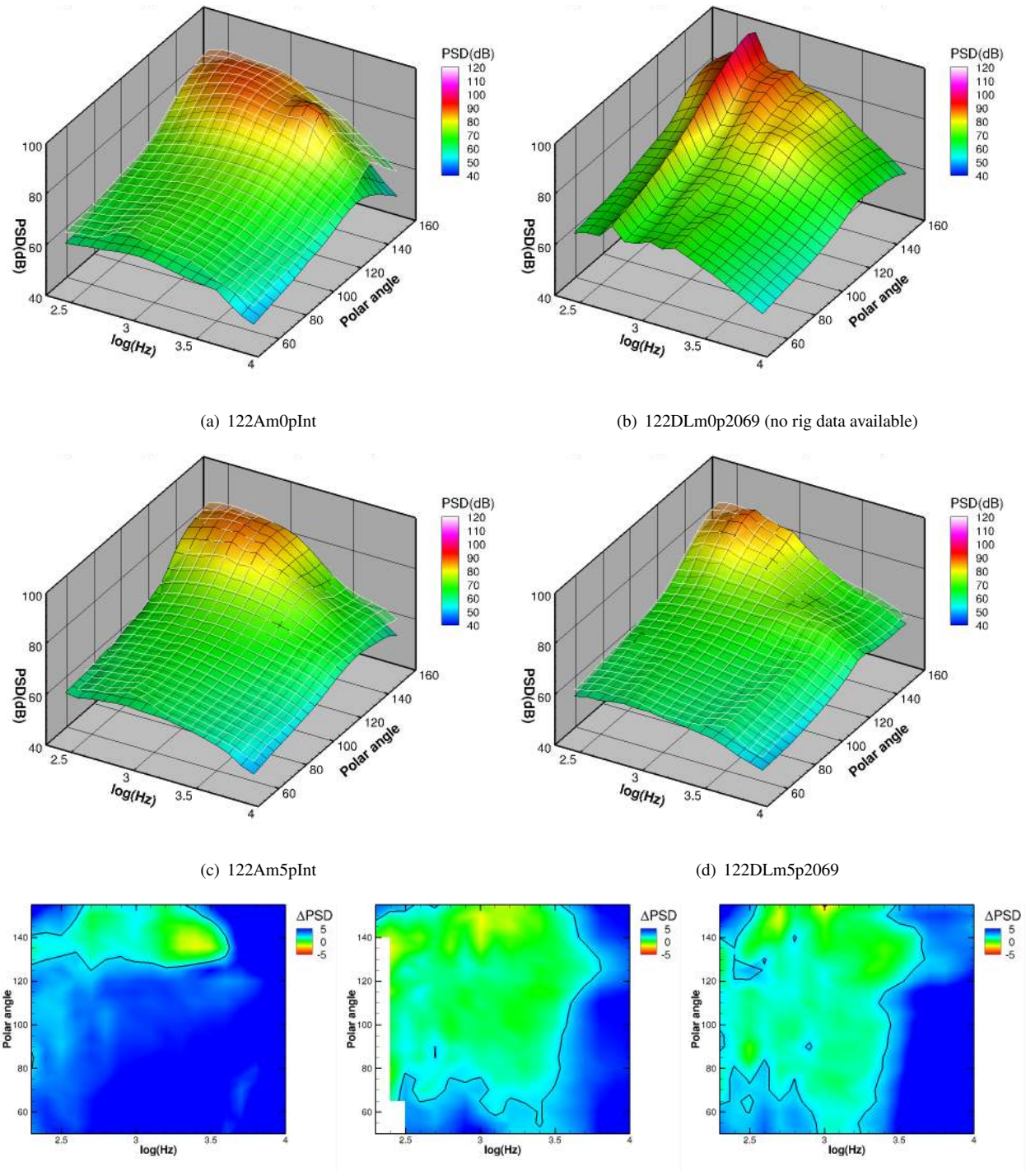

(a) 122Am0pInt

(b) 122DLm0p2069 (no rig data available)

(c) 122Am5pInt

(d) 122DLm5p2069

(e) 122Am0pInt

(f) 122Am5pInt

(g) 122DLm5p2069

Fig. 15 SP1200 [M_{ref}=0.02 ; NPR_C=1.997 ; NTR_C=3.253 ; NPR_B=1.993 ; NTR_B=1.199]. (a)-(d) Far-field spectra directivity comparison between WMLES LAVA data and rig data from [14]. The solid surfaces with black mesh represent WMLES data, while transparent surfaces with white mesh depict rig data. Panels (e)-(g) illustrate the differences between WMLES and rig data, with black contour lines representing ±2dB levels. Note: The LES data were generated for the p2069 plug, whereas experimental data were available only for the p2068 plug. This difference is expected to result in only minor discrepancies.

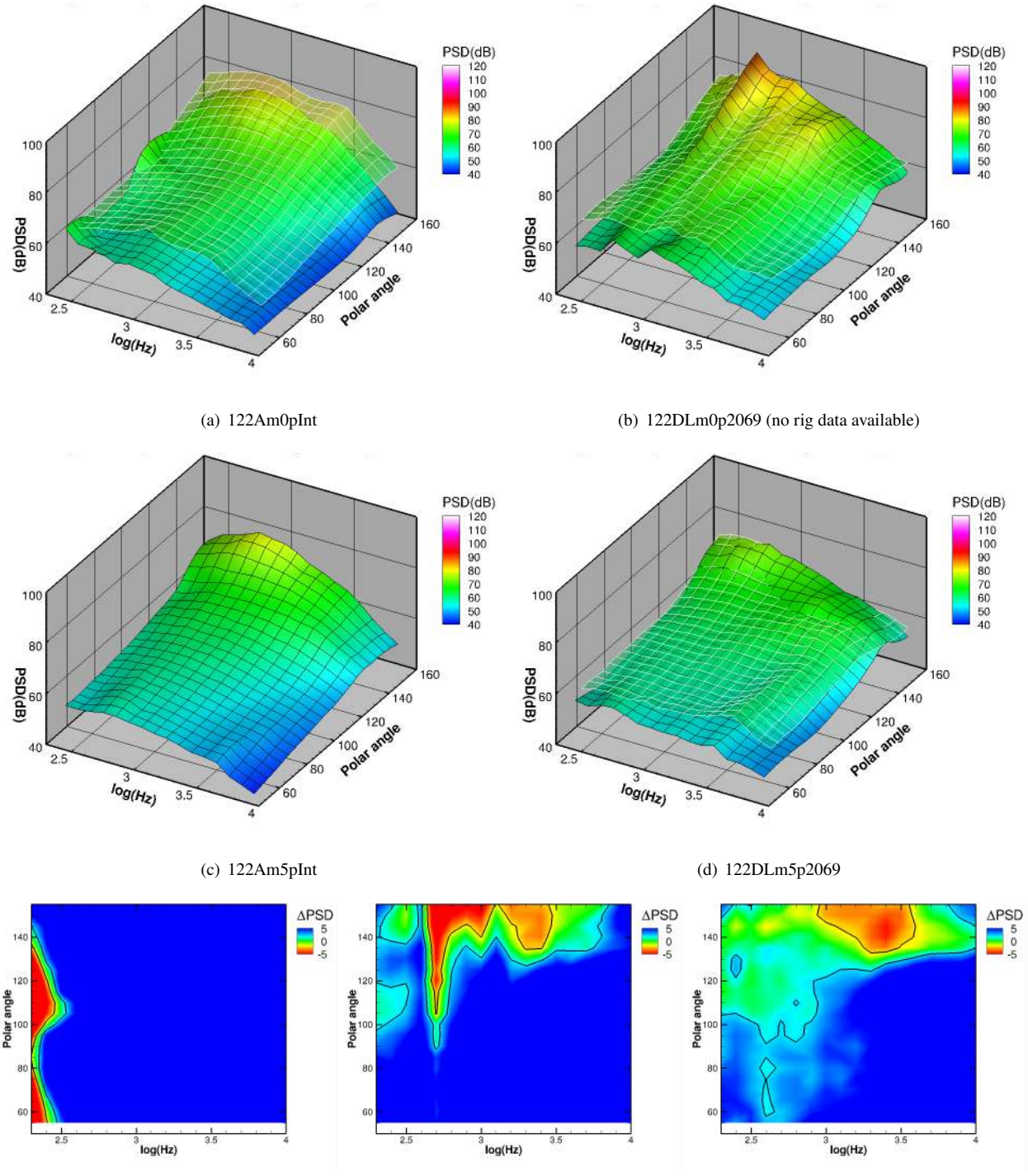

(a) 122Am0pInt

(b) 122DLm0p2069 (no rig data available)

(c) 122Am5pInt

(d) 122DLm5p2069

(e) 122Am0pInt

(f) 122DLm0p2069

(g) 122DLm5p2069

Fig. 16 SP1203 [M_{ref}=0.3 ; NPR_C=1.997 ; NTR_C=3.253 ; NPR_B=1.993 ; NTR_B=1.199]: (a)-(d) Far-field spectra directivity comparison between WMLES LAVA data and rig data from [14]. The solid surfaces with black mesh represent WMLES data, while transparent surfaces with white mesh depict rig data. Panels (e)-(g) illustrate the differences between WMLES and rig data, with black contour lines representing ±2dB levels. Note: The LES data were generated for the p2069 plug, whereas experimental data were available only for the p2068 plug. This difference is expected to result in only minor discrepancies.

upcoming journal paper. In an effort to foster effective communication within the community, we are committed to being transparent about our results, even if they are not always satisfactory. This openness is not always prevalent in literature, where results might selectively highlight successes. By sharing our complete findings, we aim to inspire open discussions and encourage a more collaborative approach to resolving complex scientific challenges. This commitment not only helps to advance our understanding but also builds trust and drives innovation in the field of aeroacoustics.

A. Impact of Gravity and Thermal Factors on Nozzle Configuration and Acoustic Emissions

First, we focus on the implications of modifying the plug geometry for the external plug 122DLmXp2069 configuration on SP1200 (M_{ref}=0.02; NPR_C=1.997; NTR_C=3.253; NPR_B=1.993; NTR_B=1.199). As detailed in Section V.A, it has been observed that the plug undergoes deformation—specifically drooping and elongation—both under heated conditions (e.g., SP1200) and in the cold state (e.g., SP7X) during the experimental campaign. In the initial phase of our investigation (Part I), we did not account for any deformations and used an axisymmetric placement centered around the nozzle's center-line. The impact of gravity and heat on the external plug configuration is illustrated in Figure 17, where the grey geometry represents the axisymmetric setup and the red plug indicates the displacement caused by the aforementioned effects, termed 122DLmXp2069Hot. Displacement was estimated from experimental PIV images, resulting in a shift of approximately 4% relative to the nozzle diameter, or 33% of the annulus. It should be noted that detailed information about the state of the plug inside the nozzle was beyond the scope of experimental campaign; thus, we extrapolated the displacement linearly from the external plug displacement measured in the PIV. Additionally, potential deformations to both the plug and internal mixer geometries, which may occur but are not accounted for in this modification, could further influence the outcomes.

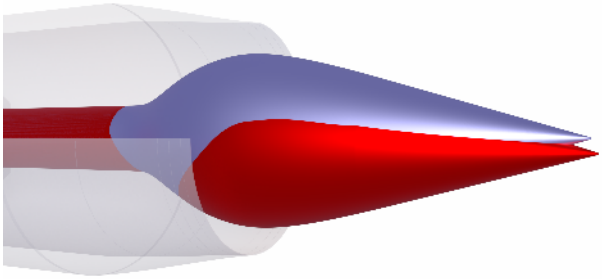

Fig. 17 Depiction of the Effects of Gravity and Heat on the 122DLmXp2069 Configuration: The grey geometry illustrates the axisymmetric configuration, while the red plug highlights the displacement resulting from the aforementioned effects. This altered configuration is designated as 122DLmXp2069Hot. Displacement estimated from experimental PIV images during the campaign.

We initially explored the impact of this displacement on the general flow field. Figure 18 presents instantaneous contour plots of streamwise velocity and temperature: the top panels (in blue) display streamwise velocity, while the bottom panels (in red) show temperature for (a) the cold axisymmetric configuration and (b) the drooped plug configuration. In figure (b), the outline of the drooped plug is accentuated with a black shade. This setup reveals a clearly asymmetric flow field akin to that observed in PIV for streamwise velocity, although this pronounced asymmetry does not appear in TKE plots.

The impact on far-field noise due to this drooping is depicted in Figure 19, showcasing noise spectra at 100D from LAVA-WMLES simulations alongside experimental results by Bridges et al. [14] (□) for angles up to 105°. This comparison includes the axisymmetric 122DLm5p2069 configuration (——) and the 122DLm5p2069Hot configuration (——), featuring the drooped and elongated plug. The drooping significantly affects noise predictions at upstream observer angles up to Θ = 105°. Observers positioned further downstream did not detect impacts from this geometric modification. Notably, with the displaced plug configuration, a slight onset of a hump in the frequency spectrum around 4000Hz is now evident, although smaller in peak magnitude compared to the experimental observation. Moreover, no impact on far-field noise at higher frequencies or observer angles beyond 105° was observed, indicating that additional plug displacements might trigger larger changes, or other experimental factors are at play. It's also plausible that the displacement caused other physical flow features like plug vibration or stronger shocks, which were not considered in

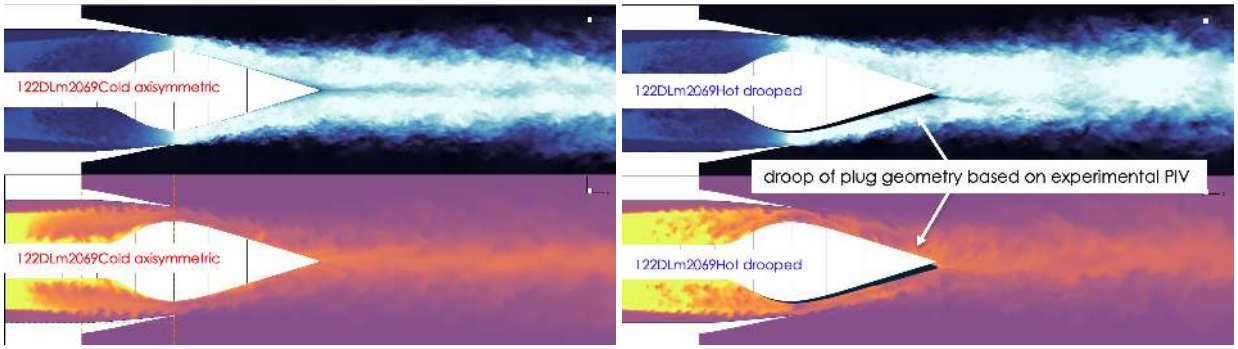

(a) SP1200 - 122DLmp2069 Cold

(b) SP1200 - 122DLmp2069 Hot

Fig. 18 Instantaneous Contour Plots of Streamwise Velocity and Temperature: The top panels (in blue) depict the instantaneous streamwise velocity, while the bottom panels (in red) show the instantaneous temperature for (a) the cold axisymmetric configuration and (b) the drooped plug configuration. In figure (b), the outline of the drooped plug is highlighted with a black shade.

our simulations.

Figure 20(a) compares the far-field spectra directivity from LES of the 122DLm5p2069 and LES of 122DLm5p2069Hot configurations. Panel (b) highlights the differences between the two simulations, notably the presence of a spectral hump at frequencies around Log(Hz)=3.5 for angles up to 105°. Black contour lines representing ±2dB levels. This shows how the drooping of the plug is focused on the upstream angles in a smaller frequency range of mid-frequencies.

Similar testing was also performed early in the study for the internal plug configuration with axisymmetric mixers, aiming to address discrepancies in low to mid-frequency far-field noise. This displacement testing was conducted before the experimental PIV campaign had revealed the displacement of the external plug. For this case, we displaced the plug approximately 10% of the nozzle diameter to break the flow symmetry, hypothesizing that this might explain the excess noise observed in experiments. Unfortunately, no significant impact on our far-field noise predictions was observed from this internal plug displacement.

B. Exploring the Acoustic Impact of Mixer Vibrations via Resonating Boundary Conditions

To explore the potential impact of mixer vibrations on the aeroacoustic environment, this subsection details our approach of applying resonating boundary conditions within our WMLES simulation. Although it is uncertain whether mixer vibrations occur in the experimental setup, we introduced a wall-normal velocity component to our existing wall-function boundary conditions, modeled as a time-dependent sine wave or a combination of sine waves, to simulate the possible effects of such vibrations.

The implemented boundary conditions utilize either a fixed frequency or a spectrum of frequencies to approximate the resonance phenomena that might be associated with structural vibrations of the internal mixer. This modification not only enhances the realism of our simulations but also allows us to investigate how hypothetical vibrations could influence noise generation and propagation. By systematically varying the frequency and amplitude of the sine waves, we explore the acoustic response of the nozzle to different vibrational states, providing insights into the potential interaction between structural dynamics and fluid flow. During this study, several configurations were tested. However, we have chosen to focus on a limited subset in this paper, with further discussion to be provided in an upcoming companion paper.

This line of investigation was initiated during the plug displacement study, prompting us to consider whether the forces distorting the solid metal plug might also affect the mixer's extremely thin geometry. It is important to note that the pressures of the two streams—core and bypass—are matched, which theoretically should prevent deformation. Nevertheless, there remains a question as to whether initial transients could excite some form of resonance within the nozzle geometry that might persist over time. Additionally, we explored whether there could be flow separation of the turbulent boundary layer on the mixer geometry in experiments that is not captured in our LES simulations. By analyzing time-averaged skin friction on the mixer geometry in LES, we confirmed that there is no persistent flow separation of the mixer in the symmetric 122DLm5p2069 configuration, although very slight, negligible, instantaneous flow separation is observable at the root of the lobes and at the very tip. This behavior is illustrated using instantaneous

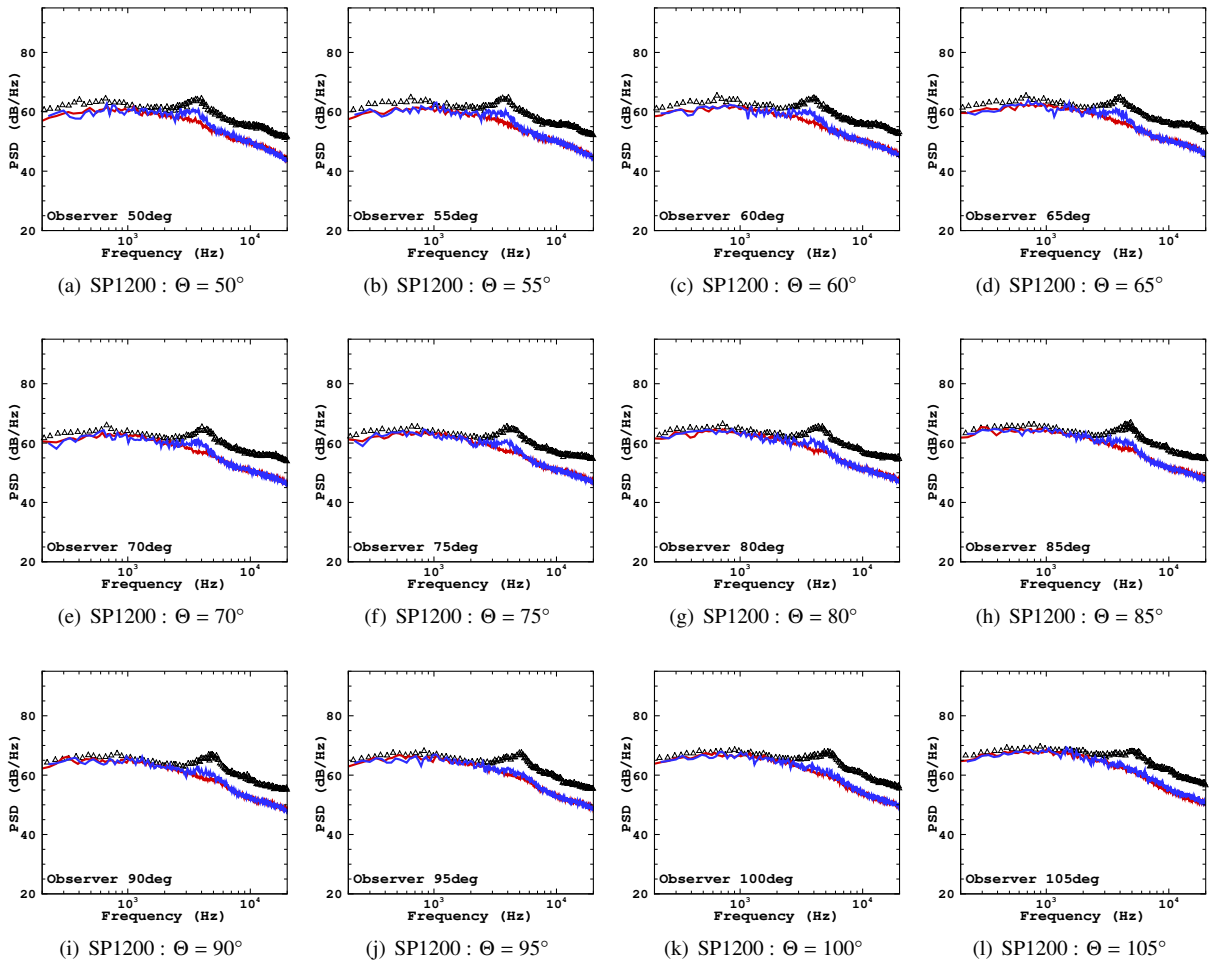

(a) SP1200 : Θ = 50° (b) SP1200 : Θ = 55° (c) SP1200 : Θ = 60° (d) SP1200 : Θ = 65°

(e) SP1200 : Θ = 70° (f) SP1200 : Θ = 75° (g) SP1200 : Θ = 80° (h) SP1200 : Θ = 85°

(i) SP1200 : Θ = 90° (j) SP1200 : Θ = 95° (k) SP1200 : Θ = 100° (l) SP1200 : Θ = 105°

Fig. 19 Noise spectra at 100D from LAVA-WMLES simulations alongside experimental results by Bridges et al. [14] (□). This comparison involves the axisymmetric 122DLm5p2069 configuration (——) and the 122DLm5p2069Hot configuration (——), which features a drooped and extended plug. The impact of the plug droop is observable in angles up to 105°; beyond this, the results from both configurations align closely.

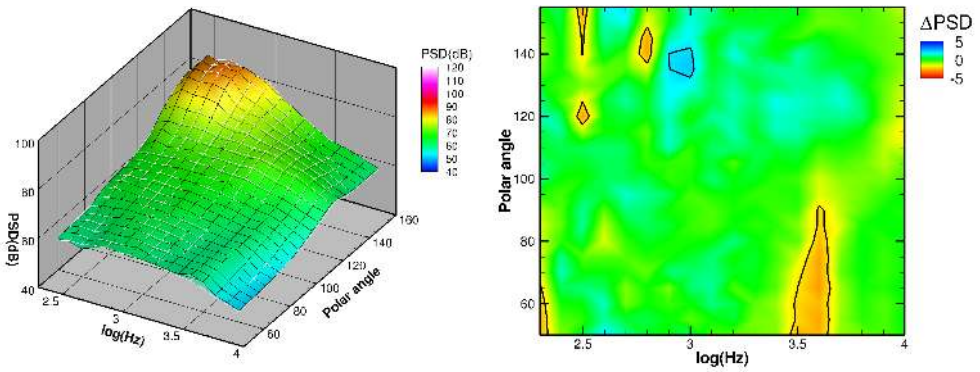

(a) 122DLm5p2069 (b) 122DLm5p2069

Fig. 20 SP1200 [M_{ref}=0.02; NPR_C=1.997; NTR_C=3.253; NPR_B=1.993; NTR_B=1.199]. This figure compares the far-field spectra directivity from LES of the 122DLm5p2069 and the 122DLm5p2069Hot configurations, which feature a drooped and elongated plug. Panel (b) highlights the differences between the two simulations, notably the presence of a spectral hump at frequencies around Log(Hz)=3.5 for angles up to 105°. Black contour lines representing ±2dB levels

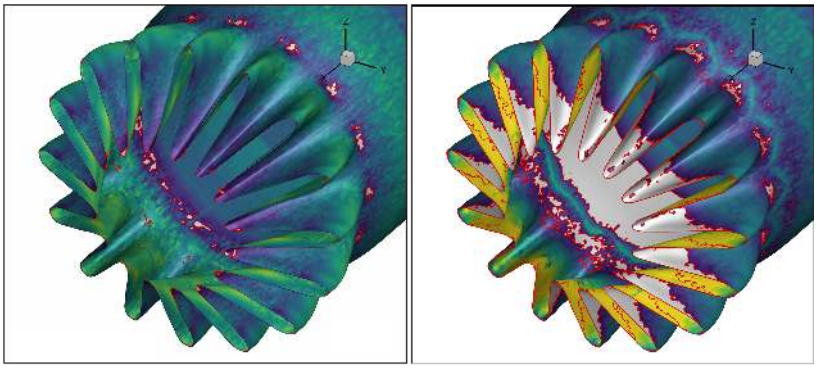

Fig. 21 Instantaneous Streamwise Velocity on the Surface of the lobed mixer for SP1183 122DLm5p2069: The left panel shows the velocity for the axisymmetric version without forcing, while the right panel displays the forced flow condition. A red contour line indicates where the velocity is zero, with velocities less than zero being clipped. This visualization highlights a distinct flow separation on the lobes in the forced case, which oscillates with the forcing frequency.

streamwise velocity in Figure 21(left), where red contour lines indicate a velocity of zero with negative velocities clipped. Furthermore, by applying a resonating wall-normal velocity, we induced significant time-dependent flow separation on the plug, as seen in Figure 21(right).

The impact of this forced resonance on the general flow field is shown in Figure 22. These images present instantaneous Contour Plots of Streamwise Velocity and Temperature: the top panels (in blue) display the instantaneous streamwise velocity, while the bottom panels (in red) show the instantaneous temperature for (a) the cold axisymmetric configuration and (b) the cold axisymmetric configuration with applied resonating boundary conditions (BCs) at 4500Hz and 5m/s. Noticeable wave-like patterns in the streamwise velocity and temperature are evident, subtly altering the mixer shear layer.

Next, we assess the impact of a specific forcing frequency on the far-field noise spectra. We demonstrate this using a single forcing frequency of 4500Hz in the wall-normal direction. It is important to note that the forcing on the inside of the mixer surface is negatively signed relative to the outside to simulate a vibration of the geometry rather than an expansion and compression of the mixer. In our study, approximately 20 different methods of forcing were tested; these will be detailed in future publications. Figure 23 displays the noise spectra at 100D from LAVA-WMLES

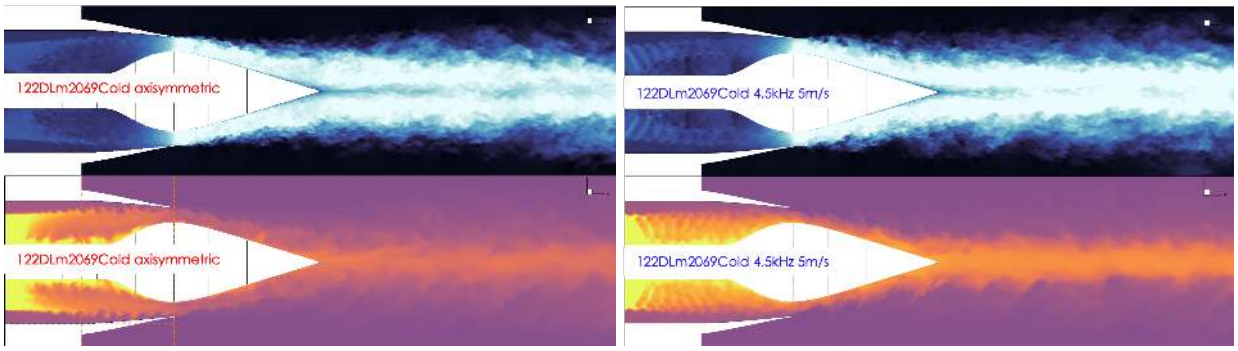

(a) SP1200 - 122DLmp2069 Cold

(b) SP1200 - 122DLmp2069 Resonating 4.5kHz 5m/s

Fig. 22 Instantaneous Contour Plots of Streamwise Velocity and Temperature: The top panels (in blue) depict the instantaneous streamwise velocity, while the bottom panels (in red) show the instantaneous temperature for (a) the cold axisymmetric configuration and (b) the cold axisymmetric configuration with applied resonating BC's of 4500Hz and 5m/s.

simulations alongside experimental results by Bridges et al. [14] (□). This comparison includes the axisymmetric 122DLm5p2069 configuration for baseline LES (——) with resonating boundary conditions (BC) at frequencies of 4500Hz with strengths of 5m/s (——) and 1.5m/s (——). This study has yielded the most substantial impact to date on aligning experimental results with simulations. The 5m/s case reveals a noticeable change in high-frequency noise, aligning very closely with experimental results. However, it also introduces a strong tone and subsequent harmonics at the exciting frequency. Across the entire range of observer angles, we now observe an increased level of high-frequency broadband noise, closely matching experimental findings.

The LES simulations with this excitation even capture features like the double hump in far-field noise at far aft-angles (e.g., $\Theta = 140°$) observed in experiments. Nevertheless, we are still unable to replicate the mid-frequency hump at lower observer angles. As discussed in Section VI.A, this hump appears to be sensitive to plug displacement and the resulting asymmetry of the flow at the nozzle exit. Although the resonance study was primarily conducted for the axisymmetric configuration, a superposition of several studies may be necessary to fully match experimental results. Trials with lower amplitude excitations at the same frequency (depicted by the blue line) did not show a rise in high-frequency noise, indicating that a sufficient level of amplification is essential.

Additionally, we experimented with applying several frequencies within a defined band (2000Hz - 6000Hz) with Gaussian filters to reduce forcing at the band's edges. However, this approach led to some cancellation effects, which did not result in any broadband amplification of the noise. Another consideration was whether initiating a resonance in the flow, as might occur during startup, could cause some of the resonance to lock into the flow and persist even after the geometric resonation ceased. To investigate this, we initialized the flow with a resonating boundary condition, then turned off the BC and allowed the flow to evolve. We divided our FWH procedure into 20 bins and analyzed the PSD noise over different sections of these bins (all, first part, middle part, last part). Our findings indicate that the broadband noise component instantly returns to its original level once we deactivate the resonating boundary condition. However, the amplified tone and its inherent harmonics take a significant amount of time to dissipate. Figure **??** compares the far-field spectral directivity from LES for the 122DLm5p2069 configuration, alongside baseline LES data and LES data incorporating a resonating boundary condition at 4500Hz and 5m/s. For clarity, tones from the resonating frequency and its subsequent harmonics have been removed in this visualization, clearly illustrating the improvements between the baseline LES and experimental comparisons due to the resonating BC.

We sampled high-frequency volumetric data every 25 RK time steps, which will be used for advanced post-processing techniques such as Spectral Proper Orthogonal Decomposition (SPOD). This dataset enables us to examine the differences in high-frequency flow fields between the resonating and baseline cases. To achieve this, we conducted a Fast Fourier Transform (FFT) on the entire volumetric data set, applied a frequency band filter, and then performed an inverse FFT to isolate frequency band-filtered pressure within a specific range—specifically between the forcing frequency of 4500Hz and the first harmonic at 6750Hz. Figure 25 illustrates Frequency-Filtered Instantaneous Pressure Contours and PSD Far-Field Noise Differences: the top panel displays the baseline configuration, the middle panel shows the configuration with forcing at 4500Hz and 5m/s, and the bottom panel presents the configuration with forcing at 4500Hz and 1m/s. On

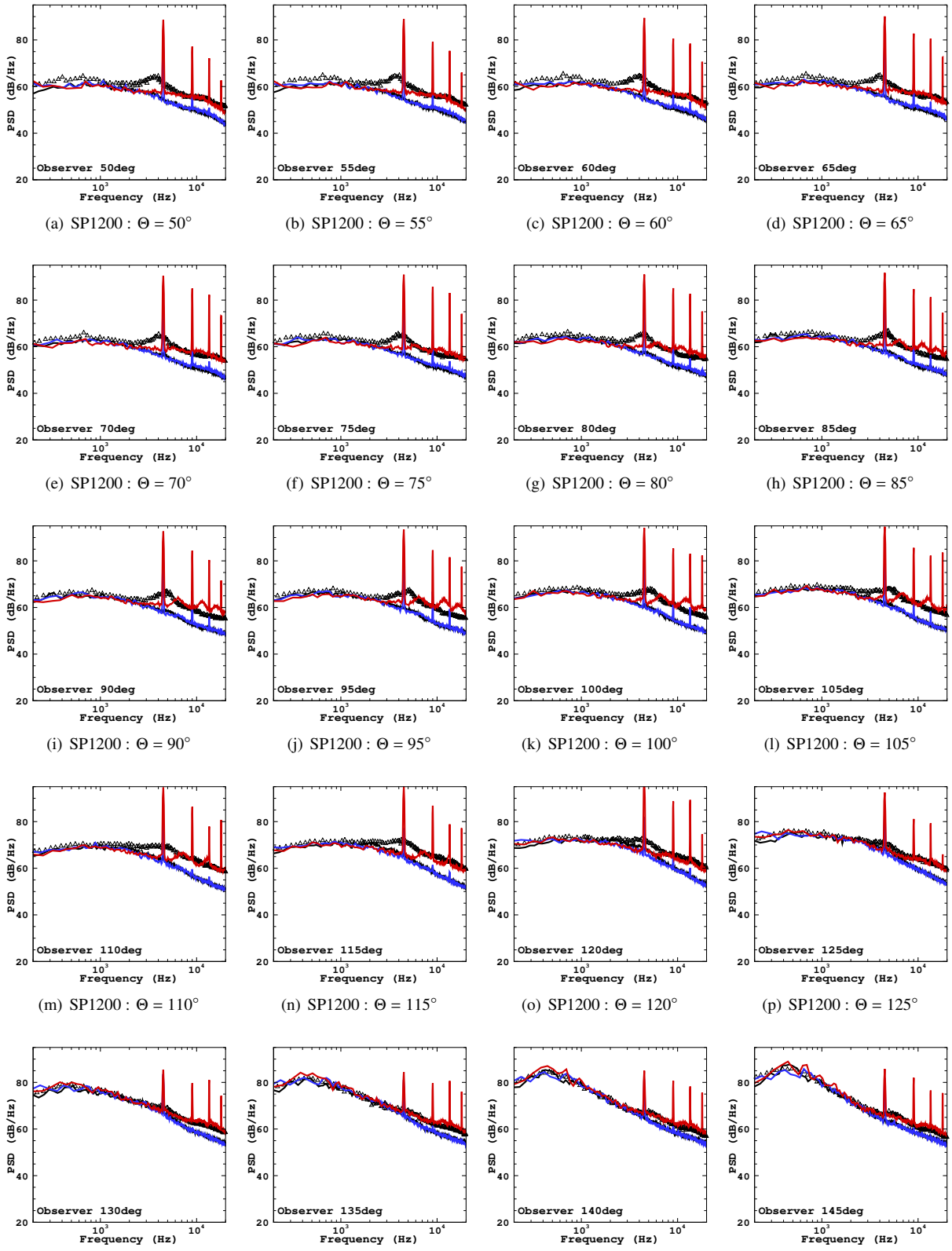

(a) SP1200 : Θ = 50° (b) SP1200 : Θ = 55° (c) SP1200 : Θ = 60° (d) SP1200 : Θ = 65°

(e) SP1200 : Θ = 70° (f) SP1200 : Θ = 75° (g) SP1200 : Θ = 80° (h) SP1200 : Θ = 85°

(i) SP1200 : Θ = 90° (j) SP1200 : Θ = 95° (k) SP1200 : Θ = 100° (l) SP1200 : Θ = 105°

(m) SP1200 : Θ = 110° (n) SP1200 : Θ = 115° (o) SP1200 : Θ = 120° (p) SP1200 : Θ = 125°

(q) SP1200 : Θ = 130° (r) SP1200 : Θ = 135° (s) SP1200 : Θ = 140° (t) SP1200 : Θ = 145°

Fig. 23 Noise spectra at 100D from LAVA-WMLES simulations alongside experimental results by Bridges et al. [14] (□). This comparison involves the axisymmetric 122DLm5p2069 configuration where baseline LES (——) resonating BC at frequency of 4500Hz and strength of 5m/s (——) and 1.5m/s (——).

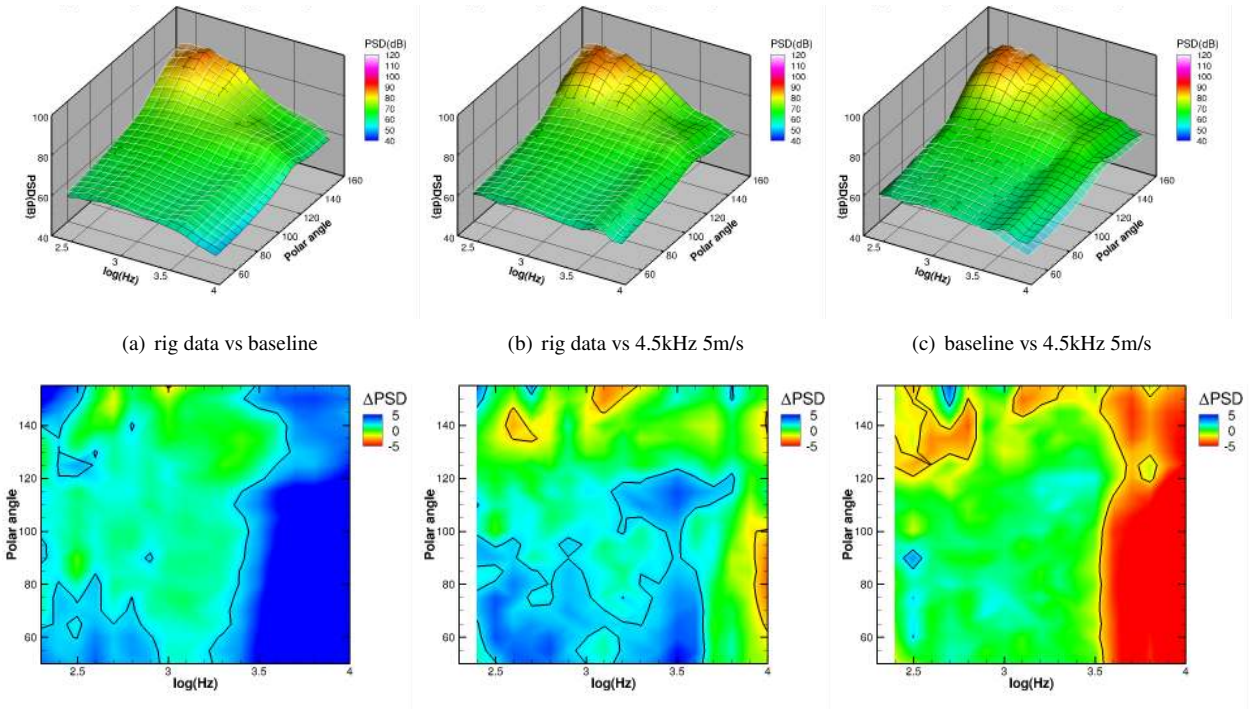

(a) rig data vs baseline (b) rig data vs 4.5kHz 5m/s (c) baseline vs 4.5kHz 5m/s

(d) rig data vs baseline (e) rig data vs 4.5kHz 5m/s (f) baseline vs 4.5kHz 5m/s

Fig. 24 SP1200 122DLm5p2069 [M_{ref}=0.02; NPR_C=1.997; NTR_C=3.253; NPR_B=1.993; NTR_B=1.199]: This figure compares the far-field spectral directivity from LES for the 122DLm5p2069 configuration, alongside baseline LES data and LES data incorporating a resonating boundary condition at 4500Hz and 5m/s. For clarity, tones from the resonating frequency and its subsequent harmonics have been removed in this visualization.

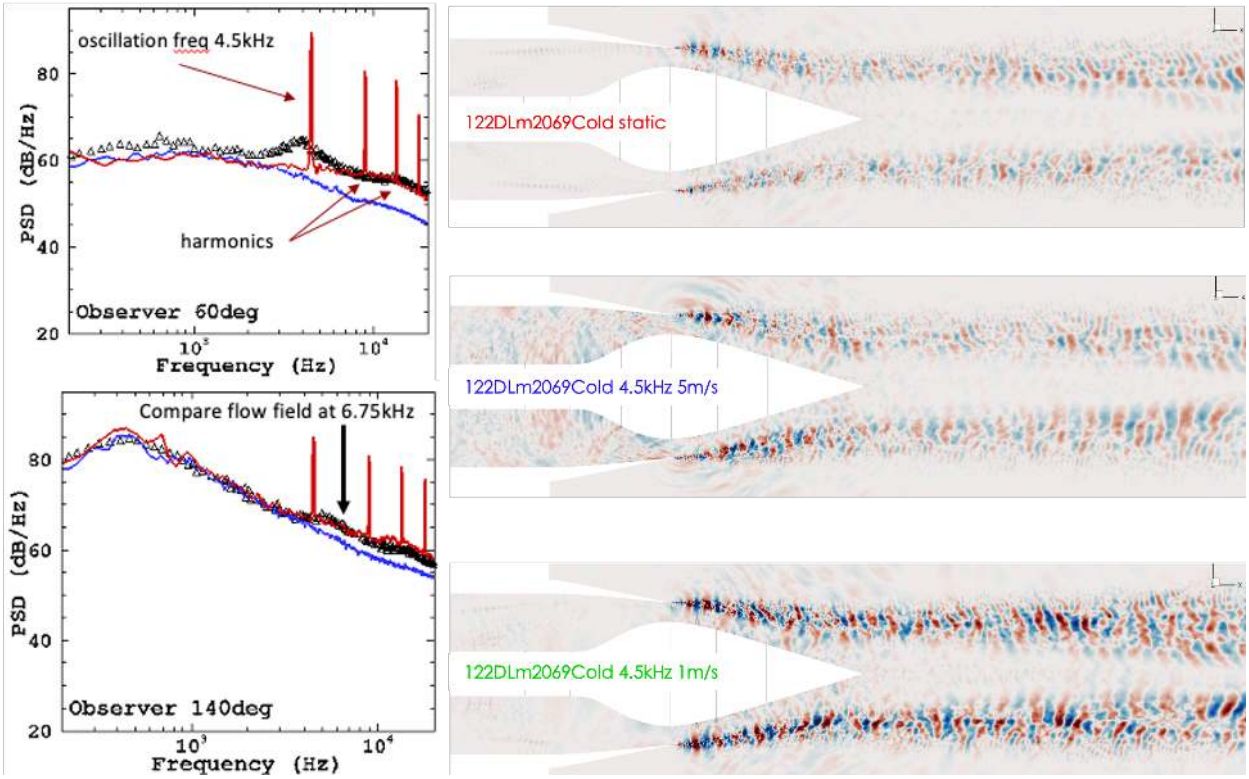

Fig. 25 Depiction of Frequency-Filtered Instantaneous Pressure Contours and PSD Far-Field Noise Differences: The top panel displays the baseline configuration, the middle panel shows forcing at 4500Hz and 5m/s, and the bottom panel presents forcing at 4500Hz and 1m/s. The figure on the left illustrates the difference in PSD far-field noise at 100Hz for two observer angles.

the left, the figure highlights differences in PSD far-field noise at 100Hz for two observer angles. A notable difference in turbulent mixing within the nozzle between the resonating and baseline configurations is evident. Additionally, the levels of turbulence in the shear layer appear to be elevated, along with an observed increase in excess noise at the nozzle lip. We plan to present more detailed findings and further analysis on these observations in future publications.

C. Enhancing Turbulence: Mesh Screens and Boundary Layer Modifications

Another aspect of our investigation focused on the influence of turbulence on the mixer geometry and the general inflow, and its impact on overall noise levels. Initially, we examined the flow features inside the nozzle generated by the lobed mixer m5 in Configuration 122DLm5p2069 at SP1200. For this, we conducted Particle Advection: passive particles were seeded at the mixer surface and advected downstream to illustrate the flow dynamics. The visualization, shown in Figure 26, reveals a clear re-laminarization of the incoming turbulent boundary layer at the mixer lobes, along with quasi-2D, strongly correlated features at the tip of the mixer lobe lip, resembling waffle cone structures. This particle advection and visualization were carried out by Timothy Sandstrom from NASA ARC, using an in-house particle advection solver. For this visualization, approximately 4.3 billion particles were in flight at all times, generating around 100TB of data. This extensive data set will also aid future efforts to perform length-scale analysis which could potentially correlate to some of the observed noise features, as well as assess the impact of turbulent mixing and boundary layer scrubbing along the inner surface.

However, in this study, we aim to highlight some initial observations about the immediate boundary layer around the mixer. It appears that the incoming turbulent boundary layer becomes laminarized at the mixer lobes, resulting in strongly correlated quasi-2D waffle cone structures in the direct vicinity of the mixer lobe lip. A key question we considered is whether this phenomenon actually occurs in experimental settings, and if not, how might a turbulent boundary layer on the mixer affect the far-field noise? These questions guide our ongoing research and experimental validation efforts.

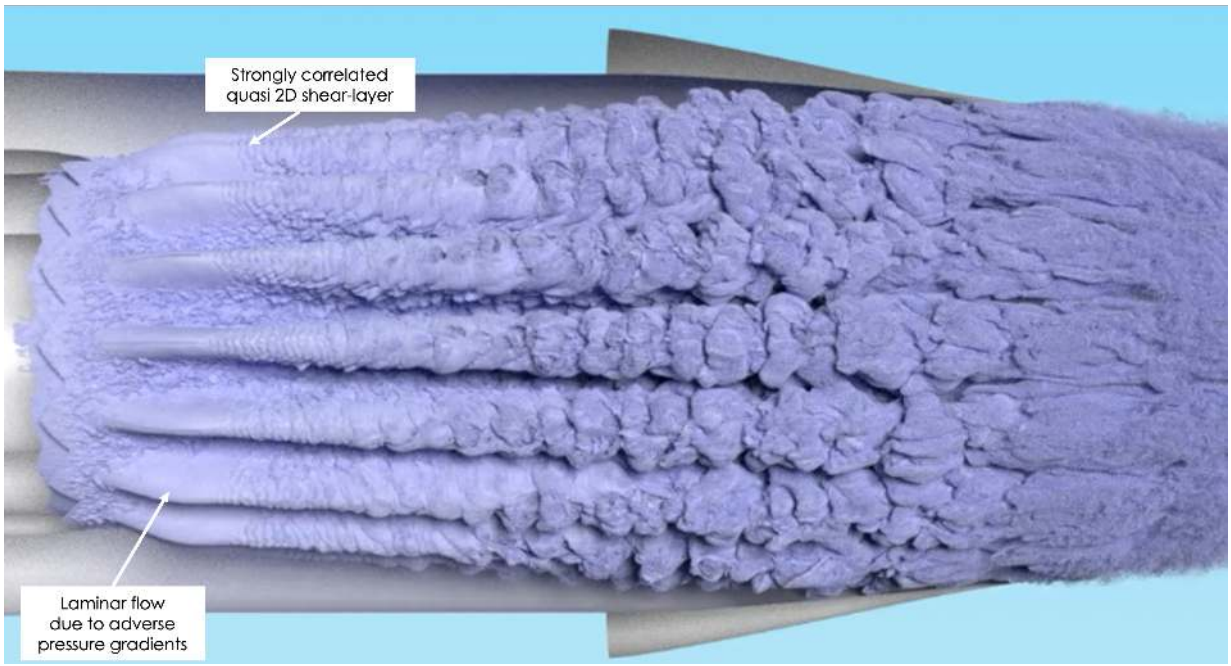

Fig. 26 Particle Advection in Configuration 122DLm5p2069 at SP1200: Passive particles were seeded at the mixer surface and advected downstream, illustrating the flow dynamics. This visualization shows a clear re-laminarization of the incoming turbulent boundary layer on the mixer lobes, as well as quasi-2D, strongly correlated features at the tip of the mixer lobe lip, resembling waffle cone structures. Particle advection and visualization were performed by Timothy Sandstrom from NASA ARC, using an in-house particle advection solver.

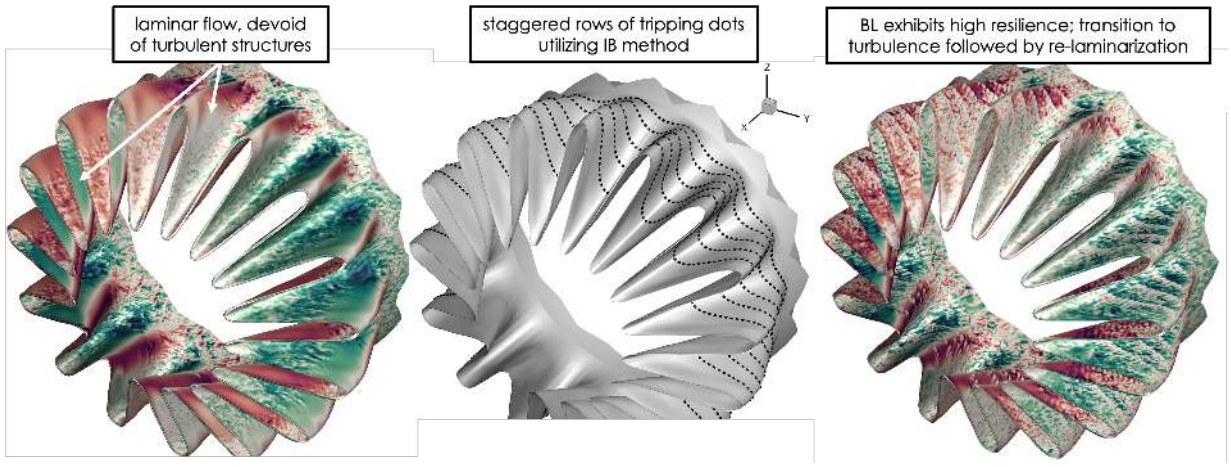

Fig. 27 Instantaneous Streamwise Velocity on the Surface of the Lobed Mixer for SP1200 122DLm5p2069: The sequence starts with the left panel displaying un-tripped flow, progresses to the middle panel featuring tripping fences, and concludes with the right panel showing the tripped state.

To tackle this issue, we expanded the application of our turbulence transition technology beyond just the nozzle inflow to generate a turbulent boundary layer (TBL). We also applied it directly on the mixer lobes to maintain turbulence throughout the flow. Our strategy involved using an immersed penalty method, where a momentum source is added to the right-hand side of the governing equation to drive the flow to zero. An associated time-scale factor determines the porosity of the immersed obstacle, with a smaller time-scale factor making it less permeable and a larger factor

making it more porous. More information on this procedure and further application can be found in Penner et.al [58] In practice, we implemented a sequence of tripping fences on the mixer geometry, as illustrated in Figure 27. This figure displays the instantaneous streamwise velocity on the surface of the lobed mixer for SP1200 122DLm5p2069. The sequence begins with the left panel showing the un-tripped flow, progresses to the middle panel with tripping fences, and concludes with the right panel depicting the flow in the tripped state. We observed a resilient boundary layer transition; despite several attempts to re-laminate due to strong adverse pressure gradients on the lobes, the boundary layer ultimately maintained a 3D turbulent structure, particularly at the mixer lip, facilitating a more rapid particle transition. Additional post-processing to generate particle visualization for comparison is currently underway. However, a comparison of the far-field noise spectra reveals that these modifications have not impacted the overall noise, as shown in Figure 29. This finding aligns with preliminary observations made for the internal plug configuration 122Am0pInt at SP1180, where we modified and rigorously tested the effect of the TBL state across several configurations. None of these alterations resulted in significant changes to the far-field noise for the plug20 configuration.

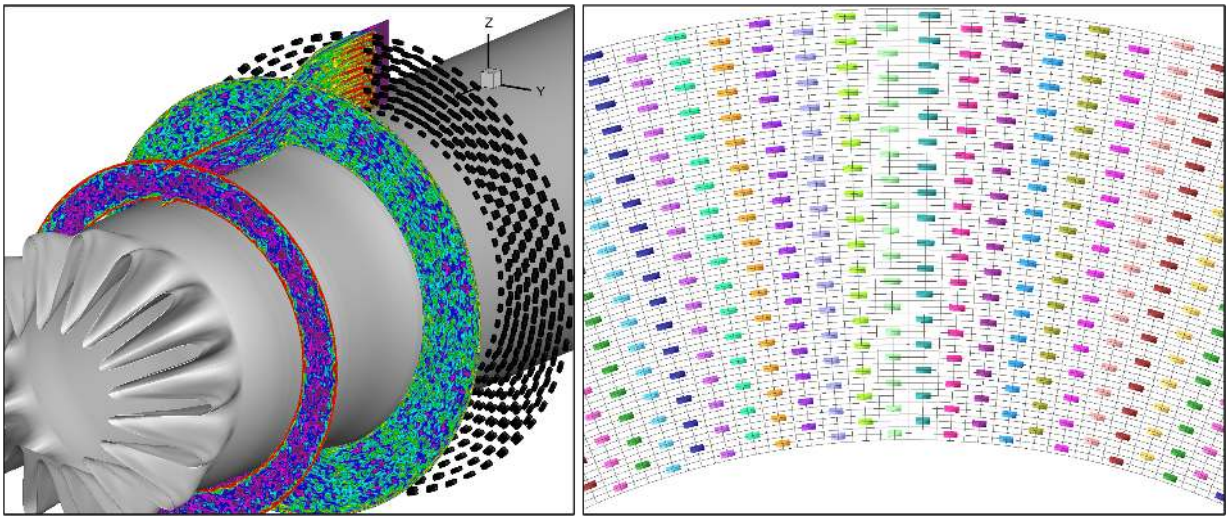

Fig. 28 Effect of inflow turbulent screen on flow-field. Left picture shows streamwise velocity on 3 different cutting planes. The tripping fences are displayed as a black iso-contour. Rigt picture shows where on the mesh the immersed boundary penalty term is applied. Every node that is inside of the tripping cylinder will have the penalty applied.

Lastly, one of our attempts to address discrepancies in the nozzle involved generating a turbulent inflow profile similar to those observed in experiments. Our study typically does not account for experimental upstream effects, such as those from pressure tabs and the plenum, and instead assumes a uniform laminar inflow profile across the domain with tripping applied near each surface to generate a turbulent boundary layer (TBL). To explore the potential benefits of a more experimentally accurate inflow condition, we modified the mesh to extend the inflow domain upstream and added a tripping mesh using our immersed boundary penalty method. Additionally, we developed a code that automatically generates these inflow disturbances, as depicted in Figure 28. The left image in the figure shows the streamwise velocity across three different cutting planes, with the tripping fences represented as black iso-contours. The right image illustrates where the immersed boundary penalty term is applied on the mesh. Every node within the tripping cylinder has the penalty applied. This modification generates a field of isotropic-homogeneous turbulence, which then propagates downstream and interacts with the general flow field. This approach aims to mimic the experimental conditions more closely and evaluate their impact on the flow dynamics and subsequent noise generation.

The effect of this turbulent inflow generation method on the flow field can be seen in Figure 30. The left panel illustrates the case with tripping on the mixer, while the right panel displays the influence of inflow turbulence generated by a inflow mesh screen utilizing the IB method. Unfortunately in the sense of getting to the bottom of the differfences with experiments this didn't result in any change to the noise as seen in Figure 29 however this is in fact a positive things as it means we do not needs to add all the additional flow featyures upstream of the typical LES inflow plane as thjis would drastically increase our simulation costs.

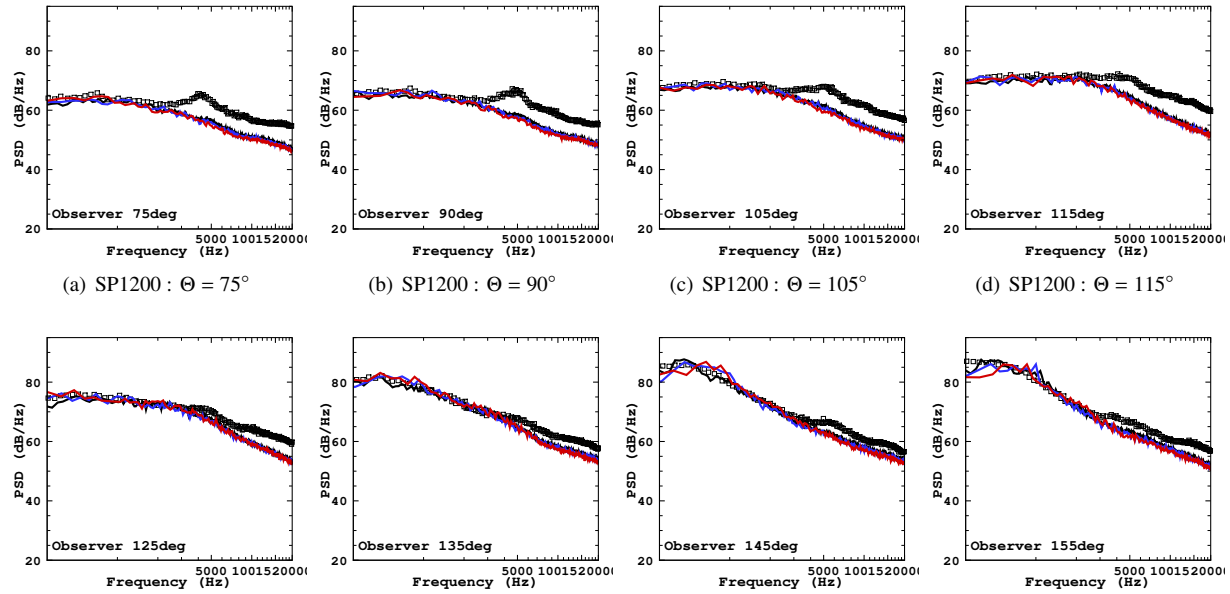

(a) SP1200 : Θ = 75° (b) SP1200 : Θ = 90° (c) SP1200 : Θ = 105° (d) SP1200 : Θ = 115°

(e) SP1200 : Θ = 125° (f) SP1200 : Θ = 135° (g) SP1200 : Θ = 145° (h) SP1200 : Θ = 155°

Fig. 29 Noise Spectra at 100D from LAVA-WMLES Simulations Compared with Experimental Results by Bridges et al. [14] (□): The figure also displays the effects of different turbulence generation mechanisms, with the inflow mesh screen shown in (——) and the mixer tripping fence in (——). The similarity in PSD spectrum, indicating a lack of sensitivity in the noise these turbulence mechanisms. The minor differences observed are attributed to the simulations for tripping not being run as long as the others.

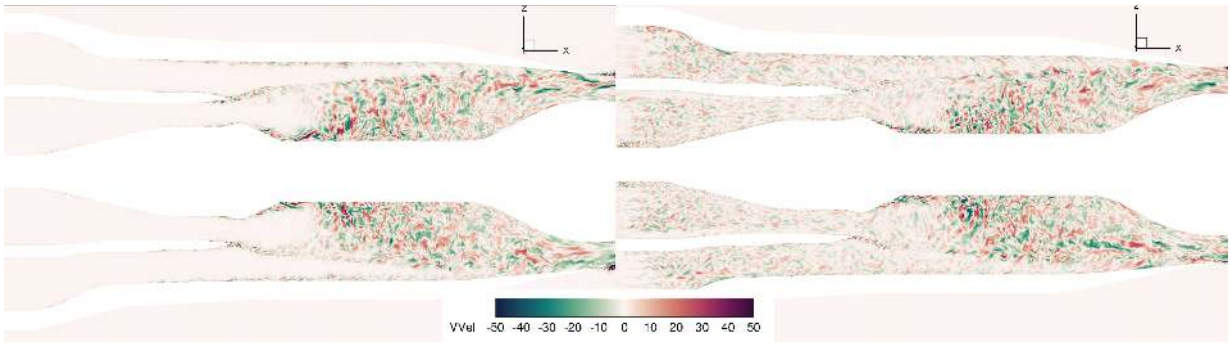

Fig. 30 Contour Plots of V-Velocity in the XZ Plane at Y=0 for 122DLm5p2069: The left panel illustrates the case with tripping on the mixer, while the right panel displays the influence of inflow turbulence generated by a inflow mesh screen utilizing the IB method.

VII. Alternative Lobed Mixer Meshing Strategy

Having explored the discrepancies between LES and experimental noise data, we now turn our attention to addressing challenges related to increasing the turnaround time for testing different configurations, specifically aiming to simplify the complex meshing process described in previous sections. Generating accurate WMLES grids for the lobed mixer introduces several complexities as outlined in Section IV. Manual mesh generation results in a 15% increase in mesh count and a 40% reduction in the time-step size due to the introduction of smaller cells in the convex valleys of the lobes. The complex geometry of the lobes further complicates the application of hyperbolic volume growth to the overlapping surface grids. To address these issues, we present a novel method for immersed boundary grid generation.

Immersed boundary approaches are well-known and commonly used in practice to avoid meshing complex geometric components [59, 60]. A requirement for immersed grids is the resolution of the geometric boundaries of the component.

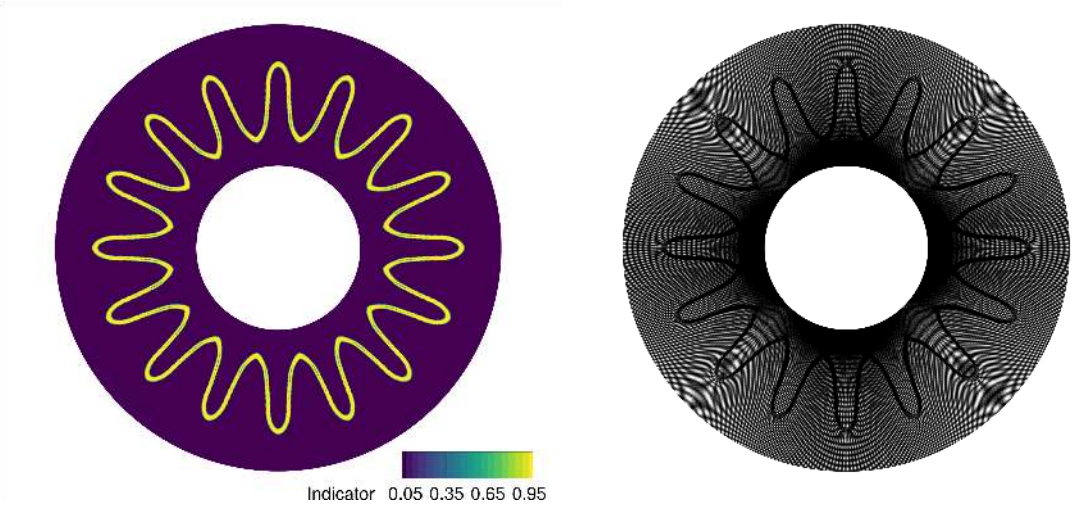

(a) Refinement indicator. (b) Refined grid.

Fig. 31 Geometry-based indicator (left) and the resulting refined grid (right).

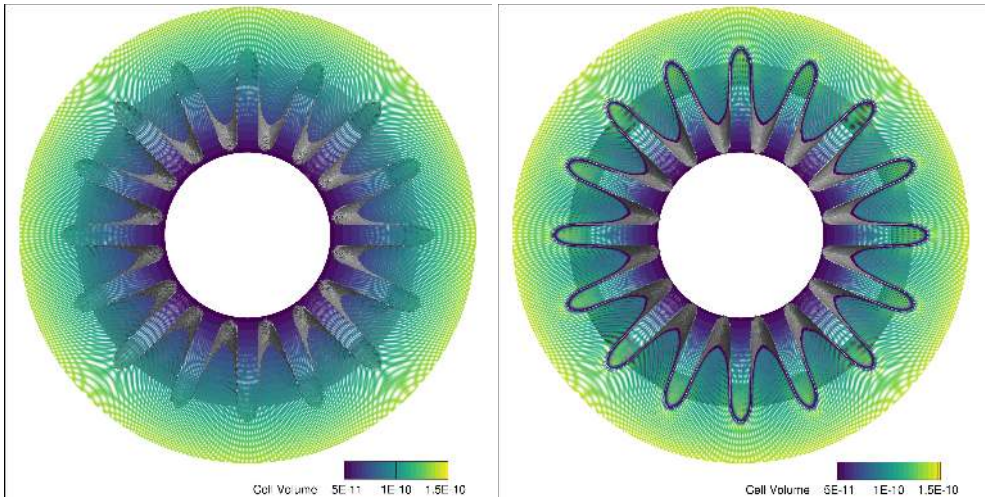

(a) Isotropic cylindrical grid. (b) Refined grid.

Fig. 32 Comparison of cell volume between the initial isotropic cylindrical and refined grids.

These boundaries are numerically identified during the preprocessing stage of CFD simulations, where each mesh point is labeled as either inside or outside the geometry. The quality of the immersed grid can be qualitatively evaluated by generating an iso-surface of the resulting marked scalar field (see Figure 33). Manual iterative refinement of these blocks may be required to remove holes and increase the smoothness of geometric resolution.

We've developed a novel geometry-based adaptation strategy for automatically resolving immersed geometry components, eliminating the need for manual iterative refinement. Let $\Omega_p \subset \mathbb{R}^3$ denote the physical space associated with an immersed boundary grid and $\Omega_c \subset \mathbb{R}^3$ the continuum computational space. Mesh redistribution is achieved through three-dimensional curvilinear elliptic adaptation equations [61–64]:

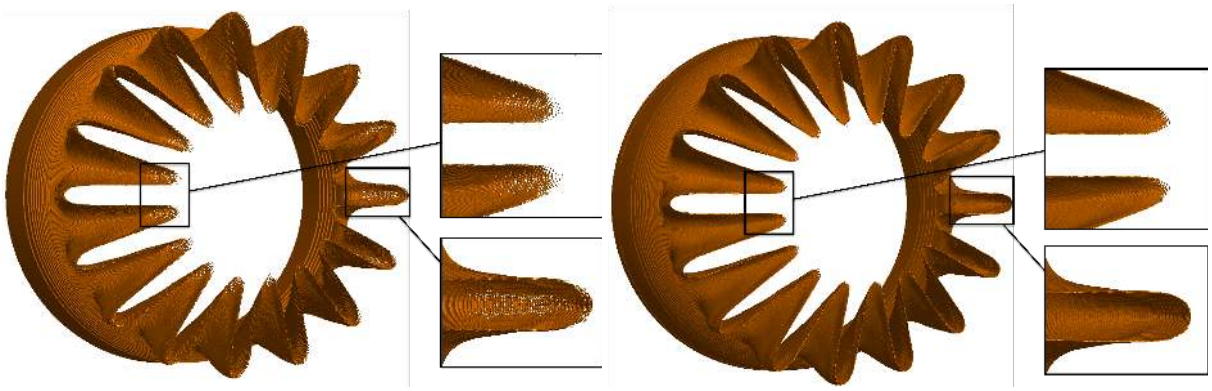

(a) Uniform (b) Refined

Fig. 33

$$\begin{aligned}\Delta\xi^1 &= \xi^1_{xx} + \xi^1_{yy} + \xi^1_{zz} = (\nabla\xi^1 \cdot \nabla\xi^1)\varphi^1 \\ \Delta\xi^2 &= \xi^2_{xx} + \xi^2_{yy} + \xi^2_{zz} = (\nabla\xi^2 \cdot \nabla\xi^2)\varphi^2 \\ \Delta\xi^3 &= \xi^3_{xx} + \xi^3_{yy} + \xi^3_{zz} = (\nabla\xi^3 \cdot \nabla\xi^3)\varphi^3\end{aligned} \tag{1}$$

where $\xi(\mathbf{x}) : \Omega_p \rightarrow \Omega_c$, $\boldsymbol{\xi} = (\xi^1, \xi^2, \xi^3)$, $\mathbf{x} = (x, y, z)$, and φ^i represents the control function for the i^{th} computational space direction. These equations are transformed to solve for redistributed physical coordinates on the computational space:

$$\sum_{i=1}^{3}\sum_{j=1}^{3} g_v(\nabla\xi^i \cdot \nabla\xi^j)\mathbf{x}_{\xi^i\xi^j} + \sum_{k=1}^{3} g_v(\nabla\xi^k \cdot \nabla\xi^k)\varphi^k\mathbf{x}_{\xi^k} = \mathbf{0} \tag{2}$$

Here, g_v represents is square of the local metric Jacobian (cell volume squared).

We employ the equidistribution control functions introduced by anderson1986 and later extended to the following general form [64]:

$$(\nabla\xi^i \cdot \nabla\xi^i)\varphi^i = \sum_{j=1}^{3} \frac{(\nabla\xi^i \cdot \nabla\xi^j)(W^i)_{\xi^j}}{W^i} \tag{3}$$

where the weights W^i are defined as functions of adaptation indicators:

$$W^i = 1 + A f_i \tag{4}$$

These indicators define the regions of clustering and coarsening, with the clustering constant A governing their strength [65]. For our novel geometry-based approach, we define special indicators targeting the boundaries of the immersed geometry. Let $i_b : \Omega_c \rightarrow [0, 1]$ be the immersed boundary function:

$$i_b(\boldsymbol{\xi}) = \begin{cases} 1 & \mathbf{x}(\boldsymbol{\xi}) \subset \partial\Omega_g \\ 0 & \text{otherwise} \end{cases} \tag{5}$$

where $\partial\Omega_g$ denotes the immersed boundary surface. The adaptation indicators are defined as follows

$$f_i(\boldsymbol{\xi}) = \nabla i_b(\boldsymbol{\xi}) \tag{6}$$

A smoothing procedure must be applied to the adaptation indicators to solve the governing adaptation equations. Details on the smoothing procedure and automatic computation of the clustering constant can be found in [66].

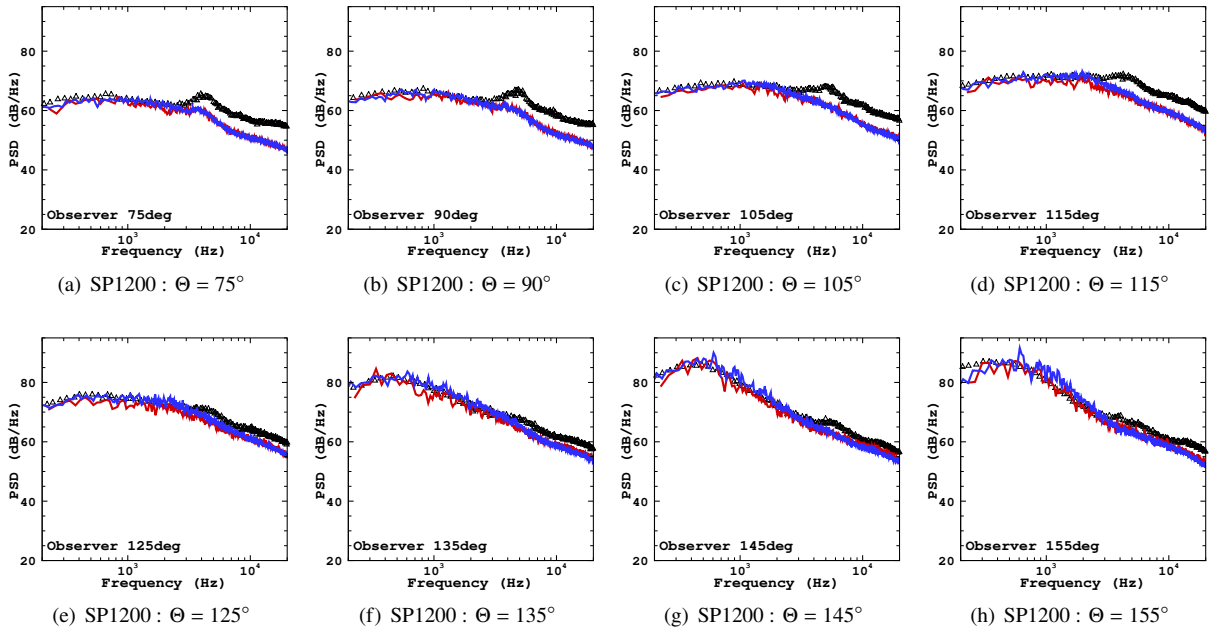

(a) SP1200 : Θ = 75° (b) SP1200 : Θ = 90° (c) SP1200 : Θ = 105° (d) SP1200 : Θ = 115°

(e) SP1200 : Θ = 125° (f) SP1200 : Θ = 135° (g) SP1200 : Θ = 145° (h) SP1200 : Θ = 155°

Fig. 34 Noise spectra at 100D from LAVA-WMLES simulations compared with experimental results by [14] (□). The figure shows results for utilizing a body-fitted mixer m5 (——) and an immersed boundary method penalty approach (——) mixer. Both simulation results utilized the 122DLm5p2069Hot geometry with drooped and extended mixer as described in Section VI.A. No major differences in noise spectra have been observed.

Based on the lobed mixer topology, we choose the initial immersed mesh to be an isotropic cylindrical mesh with sufficient starting resolution to couple with the surrounding overlapping grids. The smoothed adaptation indicator is depicted in Figure 31(a). This results in a final adapted mesh targeting the complex geometry of the lobed mixer, shown in Figure 31(b). A comparison between the initial and adapted cell volumes is presented in Figure 32. In addition to a fixed simulation cost, mesh redistribution achieves a 2X increase in mesh resolution. Comparisons of the i_b iso-surfaces are shown in Figure 33. The initial cylindrical mesh inadequately resolves the lobed mixer, resulting in several holes and a faceted (non-smooth) iso-surface. Adaptation fills these holes and results in a significantly smoother surface, except at the tips of the mixers. By increasing the clustering constant, the remaining surface could be resolved at the expense of a smaller time-step.

Geometry-based mesh redistribution eliminates the 40% reduction in time-step size and mitigates the 15% increase in mesh count. This process results in a much faster time-to-solution and CFD simulation, enhancing efficiency without sacrificing accuracy, as evidenced by the noise spectra in Figures 34 and 35. Such results suggest further exploration of this novel adaptation methodology, to be highlighted in a future journal paper.

VIII. Conclusion

In this study, we have presented a robust exploration into the challenges and intricacies of modeling supersonic jet noise, with particular focus on dual-stream nozzle configurations. By applying a combination of well-established best practices and novel investigative approaches, we aimed to refine the prediction accuracy of Computational Fluid Dynamics (CFD) simulations relative to experimental observations.

Summary of Key Findings:

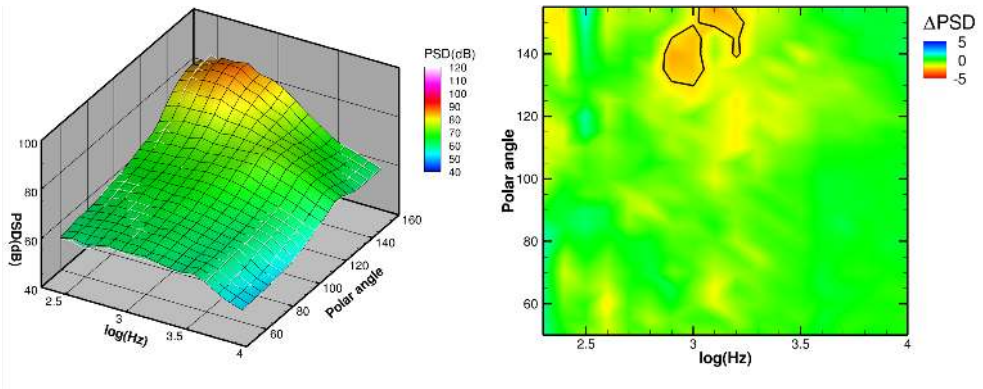

(a) 122DLm5p2069 (b) 122DLm5p2069

Fig. 35 SP1200 [M_{ref}=0.02; NPR_C=1.997; NTR_C=3.253; NPR_B=1.993; NTR_B=1.199]. This figure compares the far-field spectra directivity from LES of the 122DLm5p2069Hot and the 122DLm5p2069Hot with an immersed boundary penalty method applied to the mixer m5. Panel (b) highlights the differences between the two simulations, overall almost identical results can be observed, differences are mainly from statistical uncertainties as more averaging was applied to the Hot simulation.

- **Part I - Application of Best Practicies:** Established best practices were applied to complex supersonic nozzle configurations, revealing areas where discrepancies between simulation and experimental results persist. Benchmarking against experimental data indicated that while these practices remain robust for simpler configurations, their applicability to more complex geometries necessitates careful adjustment and enhancement.

- **Part II - Investigative Approaches into Noise Differences:** Geometric modifications, particularly addressing plug droop and mixer resonance, highlighted the significant impact of physical configuration changes on acoustic emission characteristics. Enhancements in mesh resolution and adaptation strategies facilitated a deeper understanding of the nuanced interactions between flow dynamics and acoustic behaviors, improving the fidelity of simulations. The introduction of advanced boundary conditions modeled potential physical phenomena not directly observed but plausible within the experimental setups, such as mixer vibrations and boundary layer characteristics.
- **Part III - Meshing Innovations:** The development and implementation of an immersed boundary approach for meshing complex geometries proved crucial in reducing computational costs while maintaining high-resolution data capture essential for accurate noise prediction.

Implications and Future Work: The findings from this study underscore the complex relationship between nozzle geometry, flow dynamics, and noise production in supersonic jets. The insights gained pave the way for future investigations, particularly in enhancing the predictive capabilities of simulation tools through refined modeling techniques and further experimental validations. These efforts are critical in advancing quieter propulsion systems for supersonic aircraft, addressing both regulatory requirements and public acceptance challenges. In addition we are currently assessing Structured Cartesian AMR and unstructured Voronoi mesh approaches within WMLES. Both of these approaches are fully automated and show tremendous potential in terms of prediction accuracy and reducing overall turnaround times, as the meshing is entirely automated. By sharing our methodologies, results, and challenges encountered, we contribute to the broader scientific community's understanding of supersonic jet noise. This transparency fosters a collaborative approach to research and development in the field of aeroacoustics, encouraging further studies and innovations based on our foundational work. As we continue to refine our models and approaches, future publications will delve deeper into the specific adjustments and innovations that have shown promise in bridging the gap between theoretical predictions and experimental realities. The journey towards quieter supersonic transport continues to be a dynamic and evolving field of study, demanding ongoing collaboration, innovation, and validation.

Acknowledgments

This work was partially funded by the Commercial Supersonic Technology (CST) project under the Advanced Air Vehicles Program (AAVP) and NASA's Transformational Tools and Technologies (TTT) which funded the development of tools and technologies used during this work. Our gratitude is especially extended to Gaetan Kenway and Aditya Ghate who played a crucial role in the initial stages of this research of developing WMLES capabilities. The authors would also like to thank James Bridges from NASA Glenn Research Center for his support and valuable contributions in our monthly meetings. Computer time has been provided by the NASA Advanced Supercomputing (NAS) facility at NASA Ames Research Center.

References

[1] Bridges, J. E., and Wernet, M. P., "PIV measurements of a low-noise top-mounted propulsion installation for a supersonic airliner," *AIAA Scitech 2019 Forum*, 2019, p. 0252.

[2] Bridges, J. E., "Diagnosing Noise Features of Internally Mixed, External Plug Exhaust Systems," *AIAA Aviation 2023 Forum*, 2023, p. 3210.

[3] Bridges, J. E., Wernet, M. P., Upadhyay, P., and Reising, H. H., "Flow Fields of Internally Mixed Exhaust Systems With External Plug For Supersonic Transport Applications," *AIAA AVIATION 2023 Forum*, 2023, p. 3931.

[4] Bodony, D., and Lele, S., "Current Status of Jet Noise Predictions Using Large-Eddy Simulation," *AIAA Journal*, Vol. 46, No. 2, 2008, pp. 364–380.

[5] Stich, G.-D., Housman, J. A., Kocheemoolayil, J. G., Kiris, C. C., and Bridges, J. E., "Large-Eddy Simulation of Jet Surface Interaction Noise," *25th AIAA/CEAS Aeroacoustics Conference*, 2019, p. 2475.

[6] Paliath, U., and Premasuthan, S., "Large eddy simulation for jet installation effects," *19th AIAA/CEAS Aeroacoustics Conference*, 2013, p. 2137.

[7] Housman, J., Stich, G., and Kiris, C., "Jet Noise Prediction using Hybrid RANS/LES with Structured Overset Grids," *23rd AIAA/CEAS Aeroacoustic Conference, Denver, Colorado*, 2017. AIAA-2017-3213.

[8] Stich, G.-D., Housman, J. A., Ghate, A. S., and Kiris, C. C., "Jet Noise Prediction with Large-Eddy Simulation for Chevron Nozzle Flows," *AIAA Scitech 2021 Forum*, 2021, p. 1185.

[9] Stich, G.-D., Ghate, A. S., Housman, J. A., and Kiris, C. C., "Wall Modeled Large Eddy Simulations for NASA's jet noise consensus database of single-stream, round, convergent jets." *AIAA SCITECH 2022 Forum*, 2022, p. 0684.

[10] Stich, G.-D., Ghate, A. S., Housman, J. A., and Kiris, C. C., "Wall-Modeled Large-Eddy Simulation of Jet Noise in Flight Conditions," *28th AIAA/CEAS Aeroacoustics 2022 Conference*, 2022, p. 3002.

[11] Bres, G., Nichols, J., Lele, S., and Ham, F., "Large Eddy Simulation for Jet Noise: the Importance of Getting the Boundary Layer Right," *21st AIAA/CEAS Aeroacoustics Conference, Dallas, Texas*, 2015. AIAA-2015-2535.

[12] Jordan, P., and Colonius, T., "Wave Packets and Turbulent Jet Noise," *Annual Review of Fluid Mechanics*, Vol. 45, 2013, pp. 173–195.

[13] Ingraham, D., and Bridges, J., "Validating a Monotonically-Integrated Large Eddy Simulation Code for Subsonic Jet Acoustics," *55th AIAA Aerospace Sciences Meeting, Grapevine, Texas*, 2017. AIAA-2017-0456.

[14] Bridges, J., Podboy, G., and Wernet, M., "Plug20 Test Report," *NASA Technical Manuscript*, 2021. NASA/TM-20210010291.

[15] Bridges, J., and Brown, C., "Parametric Testing of Chevrons on Single Flow Hot Jets," Tech. Rep. NASA/TM-2004-213107, National Aeronautics and Space Administration, 2004.

[16] Brown, C., and Wernet, M., "Jet-Surface Interaction Test: Flow Measurement Results," *20th AIAA/CEAS Aeroacoustics Conference*, 2014. AIAA 2014-3198.

[17] Brown, C., "Jet-Surface Interaction Test: Far-Field Noise Results," *Proceedings of the ASME Turbo Expo 2012, Copenhagen, Denmark*, 2012.

[18] Bridges, J. E., Stephens, D., and Berton, J. J., "Quantifying uncertainty of landing and takeoff noise for commercial supersonic aircraft," *28th AIAA/CEAS Aeroacoustics 2022 Conference*, 2022, p. 3051.

[19] Kiris, C., Housman, J., Barad, M., Brehm, C., Sozer, E., and Moini-Yekta, S., "Computational Framework for Launch, Ascent, and Vehicle Aerodynamics (LAVA)," *Aerospace Science and Technology*, Vol. 55, 2016, pp. 189–219.

[20] Gottlieb, S., and Shu, C.-W., "Total variation diminishing Runge-Kutta schemes," *Mathematics of computation*, Vol. 67, No. 221, 1998, pp. 73–85.

[21] Steger, J., and Benek, J., "On the Use of Composite Grid Schemes in Computational Aerodynamics," Technical Memorandum 88372, NASA, 1986.

[22] Chan, W., "Developments in Strategies and Software Tools for Overset Structured Grid Generation and Connectivity," *20th AIAA Computational Fluid Dynamics Conference, Honolulu, Hawaii*, 2011. AIAA-2011-3051.

[23] Stich, G.-D., Housman, J., Kocheemoolayil, J., Barad, M., and Kiris, C., "Application of Lattice Boltzmann and Navier-Stokes Methods to NASA's Wall Mounted Hump," *AIAA Aviation Forum, Atlanta, Georgia*, 2018.

[24] Housman, J., Stich, G., and Kiris, C., "Predictions of Slat Noise from the 30P30N at High Angles of Attack using Zonal Hybrid RANS-LES," *AIAA/CEAS Aeroacoustics Conference*, 2019.

[25] Ghate, A. S., Housman, J. A., Stich, G.-D., Kenway, G., and Kiris, C. C., "Scale Resolving Simulations of the NASA Juncture Flow Model using the LAVA Solver," *AIAA Aviation 2020 Forum*, 2020.

[26] Ghate, A. S., Kenway, G., Stich, G.-D., Browne, O., Housman, J., and Kiris, C. C., "Transonic lift and drag predictions using Wall-Modelled Large Eddy Simulations," *AIAA Scitech 2021 FORUM*, 2021.

[27] Brehm, C., Barad, M., Housman, J., and Kiris, C., "A Comparison of Higher-Order Finite-Difference Shock Capturing Schemes," *Computers & Fluids*, Vol. 122, 2015, pp. 184–208.

[28] Shu, C.-W., "High Order Weighted Essentially Nonoscillatory Schemes for Convection Dominated Problems," *SIAM Review*, Vol. 51, No. 1, 2009, pp. 92–126.

[29] Deng, X., and H., Z., "Developing High-Order Weighted Compact Nonlinear Schemes," *Journal of Computational Physics*, Vol. 165, 2000, pp. 22–44.

[30] Deng, X., Mao, M., Jiang, Y., and Liu, H., "New High-Order Hybrid Cell-Edge and Cell-Node Weighted Compact Nonlinear Schemes," *20th AIAA Computational Fluid Dynamics Conference, Honolulu, Hawaii*, 2011. AIAA-2011-3857.

[31] Housman, J., Kiris, C., and Hafez, M., "Preconditioned methods for simulations of low speed compressible flows," *Computers & Fluids*, Vol. 38, No. 7, 2009, pp. 1411–1423.

[32] Deng, X., Mao, M., Tu, G., Liu, H., and Zhang, H., "Geometric Conservation Law and Applications to High-Order Finite Difference Schemes with Stationary Grids," *Journal of Computational Physics*, Vol. 230, 2011, pp. 1100–1115.

[33] Nonomura, T., and Fujii, K., "Robust Explicit Formulation of Weighted Compact Nonlinear Scheme," *Computers & Fluids*, Vol. 85, 2013, pp. 8–18.

[34] Thornber, B., Mosedale, A., Drikakis, D., Youngs, D., and Williams, R. J., "An improved reconstruction method for compressible flow with low Mach number features," *Theoretical and Computational Fluid Dynamics*, Vol. 26, 2012, pp. 523–550.

[35] Housman, J., and Kiris, C., "Slat Noise Predictions using Higher-Order Finite-Difference Methods on Overset Grids," *22nd AIAA/CEAS Aeroacoustic Conference, Lyon, France*, 2016. AIAA-2016-2963.

[36] Musker, A., "Explicit expression for the smooth wall velocity distribution in a turbulent boundary layer," *AIAA Journal*, Vol. 17, No. 6, 1979, pp. 655–657.

[37] Bocquet, S., Sagaut, P., and Jouhaud, J., "A compressible wall model for large-eddy simulation with application to prediction of aerothermal quantities," *Physics of fluids*, Vol. 24, No. 6, 2012, p. 065103.

[38] Larsson, J., Kawai, S., Bodart, J., and Bermejo-Moreno, I., "Large eddy simulation with modeled wall-stress: recent progress and future directions," *Mechanical Engineering Reviews*, Vol. 3, No. 1, 2016, pp. 15–00418.

[39] Nicoud, F., Toda, H. B., Cabrit, O., Bose, S., and Lee, J., "Using singular values to build a subgrid-scale model for large eddy simulations," *Physics of Fluids*, Vol. 23, No. 8, 2011, p. 085106.

[40] Bose, S. T., and Park, G. I., "Wall-modeled large-eddy simulation for complex turbulent flows," *Annual review of fluid mechanics*, Vol. 50, 2018, pp. 535–561.

[41] Penner, D. C., Housman, J., Stich, G.-D., Koch, J., and Duensing, J., "Wall-Modeled Large-Eddy Simulations of a Swept Wing," *AIAA SciTech Forum and Exposition*, 2024.

[42] Uzun, A., Lyrintsis, A., and Blaisdell, G., "Coupling of integral acoustic methods with LES for jet noise prediction," *International journal of Aeroacoustics*, Vol. 3, 2004.

[43] Aikens, K., Dhamankar, N., Martha, C., Situ, Y., Blaisdell, G., Lyrintzis, A., and Li, Z., "Equilibrium Wall Model for Large Eddy Simulations of Jets for Aeroacoustics," *52nd AIAA Aerospace Sciences Meeting, National Harbor, Maryland*, 2014. AIAA-2014-0180.

[44] Aikens, K., Blaisdell, G., and Lyrintzis, A., "Analysis of Converging-Diverging Beveled Nozzle Jets Using Large Eddy Simulation with a Wall Model," *53rd AIAA Aerospace Sciences Meeting, Kissimmee, Florida*, 2015. AIAA-2015-0509.

[45] Bogey, C., and Marsden, O., "A Study of the Grid Dependence of the Flow Field and Noise of Subsonic Jets," *54th AIAA Aerospace Science Meeting, San Diego, Ca*, 2016. AIAA-2016-0261.

[46] Bres, G., Nichols, J., Lele, S., and Ham, F., "Towards Best Practices for Jet Noise Predictions with Unstructured Large Eddy Simulations," *42nd AIAA Fluid Dynamics Conference, New Orleans, Louisiana*, 2012. AIAA-2012-2965.

[47] Bres, G., Jordan, P., Jaunet, V., Ke Rallic, M., Cavalieri, A., Towne, A., Lele, S., Colonius, T., and Schmidt, O., "Importance of nozzle-exit boundary-layer state in subsonic turbulent jets," *Journal of Fluid Mechanics*, Vol. 851, 2018, pp. 83–124.

[48] Bogey, C., and Bailly, C., "Influence of nozzle-exit boundary-layer conditions on the flow and acoustic fields of initialllz laminar jets," *Journal of Fluid Mechanics*, Vol. 10, 2010, pp. 507–538.

[49] Wong, M. L., K. Kenway, G., Ghate, A. S., Stich, G.-D., and Kiris, C. C., "Predictions of LAGOON Nose Landing Gear Flow and Noise using Wall-Modeled Large Eddy Simulations," *28th AIAA/CEAS Aeroacoustics 2022 Conference*, 2022, p. 2850.

[50] S. Fernandes, L., A. Housman, J., Stich, G.-D., and C. Duensing, J., "Fan Noise Predictions of the NASA Source Diagnostic Test using Unsteady Simulations with LAVA Part II - Tonal and Broadband Noise Assessment," , 2024. To be published at the 30th AIAA/CEAS Aeroacoustics Conference.

[51] Rahier, G., Prieru, J., Vuillot, F., and Biancherin, A., "Investigation of integral surface formulations of acoustic predictions of hot jets starting from unsteady aerodynamic simulations," 2003. AIAA-2003-3164.

[52] Shur, M., Spalart, P. R., and Strelets, M., "Noise prediction for increasingly complex jets, Part 1 Methods and Tests," *International Journal of Aeroacoustics*, Vol. 4, 2005, pp. 213–246.

[53] Shur, M., Spalart, P. R., and Strelets, M., "Noise prediction for increasingly complex jets, Part 2 Applications," *International Journal of Aeroacoustics*, Vol. 4, 2005, pp. 247–266.

[54] Mendez, S., Shoeybi, M., Sharma, A., Ham, F., Lele, S., and Moin, P., "Large-Eddy Simulations of Perfectly-Expanded Supersonics Jets: Quality Assessment and Validation," *48th AIAA Aerospace Sciences Meeting, Orlando, Florida*, 2010. AIAA-2010-271.

[55] Lockard, D., "A Comparison of Ffowcs Williams-Hawkings Solvers for Airframe Noise Applications," *8th AIAA/CEAS Aeroacoustics Conference & Exhibit, Breckenridge, Colorado*, 2002. AIAA-2002-2580.

[56] Spalart, P. R., and Shur, M., "Variants of the Ffowcs Williams-Hawkings Equation and their Coupling with Simulations of Hot Jets," *International Journal of Aeroacoutics*, Vol. 8, No. 5, 2009, pp. 477–492.

[57] Mendez, S., Shoeybi, M., Lele, S., and Moin, P., "On the use of the Ffowcs Williams-Hawkings Equation to Predict Far-Field Jet Noise from Large Eddy-Simulations," *International Journal of Aeroacoustics*, Vol. 12, 2013.

[58] Craig Penner, D. A., Housman, J. A., Stich, G.-D., Sousa, V. C. B., Koch, J. R. L., and Duensing, J. C., "Wall-Modeled Large-Eddy Simulations of a Swept Wing with Leading-Edge Ice," *AIAA AVIATION 2024 FORUM*, American Institute of Aeronautics and Astronautics, 2024.

[59] Peskin , C., "Peskin, C.S.: The immersed boundary method. Acta Numerica 11, 479-517," *Acta Numerica*, Vol. 11, 2002, pp. 479 – 517. https://doi.org/10.1017/S0962492902000077.

[60] Ghate, A. S., Stich, G.-D., Kenway, G. K., Housman, J. A., and Kiris, C. C., *A Wall-Modeled LES Perspective for the High Lift Common Research Model Using LAVA*, ???? https://doi.org/10.2514/6.2022-3434, URL https://arc.aiaa.org/doi/abs/10.2514/6.2022-3434.

[61] Thompson, J. F., "Elliptic grid generation," *Applied Mathematics and Computation*, Vol. 10-11, 1982, pp. 79–105. https://doi.org/https://doi.org/10.1016/0096-3003(82)90188-6, URL https://www.sciencedirect.com/science/article/pii/0096300382901886.

[62] Eiseman, P. R., "Adaptive grid generation," *Computer Methods in Applied Mechanics and Engineering*, Vol. 64, No. 1, 1987, pp. 321–376. https://doi.org/https://doi.org/10.1016/0045-7825(87)90046-6, URL https://www.sciencedirect.com/science/article/pii/0045782587900466.

[63] Anderson, D., and Steinbrenner, J., *Generating adaptive grids with a conventional grid scheme*, ???? https://doi.org/10.2514/6.1986-427, URL https://arc.aiaa.org/doi/abs/10.2514/6.1986-427.

[64] Anderson, D. A., "Equidistribution schemes, poisson generators, and adaptive grids," *Applied Mathematics and Computation*, Vol. 24, No. 3, 1987, pp. 211–227. https://doi.org/https://doi.org/10.1016/0096-3003(87)90085-3, URL https://www.sciencedirect.com/science/article/pii/0096300387900853.

[65] Nakahashi, K., and Deiwert, G. S., "Three-dimensional adaptive grid method," *AIAA Journal*, Vol. 24, No. 6, 1986, pp. 948–954. https://doi.org/10.2514/3.9369, URL https://doi.org/10.2514/3.9369.

[66] Ashby, C., Housman, J. A., and Duensing, J. C., *Anisotropic Mach Cone Aligned Mesh Adaptation for Low Boom Simulations*, ???? https://doi.org/10.2514/6.2023-4333, URL https://arc.aiaa.org/doi/abs/10.2514/6.2023-4333.